Measurements of an axisymmetric hypersonic shear-layer instability on a cone-cylinder-flare in quiet flow

Elizabeth K. Benitez and Matthew P. Borg

High-Speed Aerodynamics Branch, Air Force Research Laboratory, Wright-Patterson Air Force Base, Ohio 45433, USA

Pedro Paredes

National Institute of Aerospace, Hampton, Virginia 23666, USA

Steven P. Schneider and Joseph S. Jewell

School of Aeronautics and Astronautics, Purdue University, West Lafayette, Indiana 47907, USA

Instabilities generated in Mach-6 quiet flow about an axisymmetric cone-cylinder-flare geometry with a 5° half-angle sharp cone were studied in the Boeing/AFOSR Mach-6 Quiet Tunnel (BAM6QT). A small, 3.5° flare angle was initially tested to provide a baseline with a model that introduces a compression to the flow but does not induce a separation. A 10° flare was then used to make measurements with an axisymmetric separation bubble. Surface heat flux and pressure fluctuation measurements were made with IR thermography and PCB and Kulite pressure sensors, respectively. Off-the-surface density gradient fluctuations were observed using focused laser differential interferometry for the separated flow. Quiet-flow measurements resulted in laminar boundary layers through the downstream edge of both models. The shear layer was found to be mostly steady in space under quiet flow, as opposed to large spatial fluctuations seen in imagery from conventional noise tunnels. In addition to the second mode, a traveling instability was observed which, based on computational analysis, corresponds to oblique waves that are amplified by the shear layer above the separation bubble. This instability was found to phase lock with the second mode as it propagates downstream. Artificial perturbations were then introduced to the 10° flare model upstream of the separation to study the resulting wave packets as they moved through the shear and boundary layers. This paper provides measurements that may be comparable to hypersonic flight due to the low-disturbance environment of the test facility.

I. INTRODUCTION

A. Shock–boundary-layer interactions (SBLIs)

Shock–boundary-layer interactions (SBLIs) occur commonly with supersonic and hypersonic vehicles. They can develop in external as well as internal flows and result in complex flow structures that are difficult to compute. When a shock encounters a boundary layer, it is affected by the viscous and rotational effects of that layer, while the boundary layer must traverse a strong adverse pressure gradient upon meeting the shock. With a compression corner in the flow, an oblique shock forms above the compression. This shock results in an adverse pressure gradient that decelerates the flow going through it; this deceleration causes a thickening of the boundary layer. As the boundary layer gets larger, it can act as a further source of compression, forming compression waves in the flow, which join to form the shock in the first place. Therefore, SBLIs create a complex, coupled problem [1].
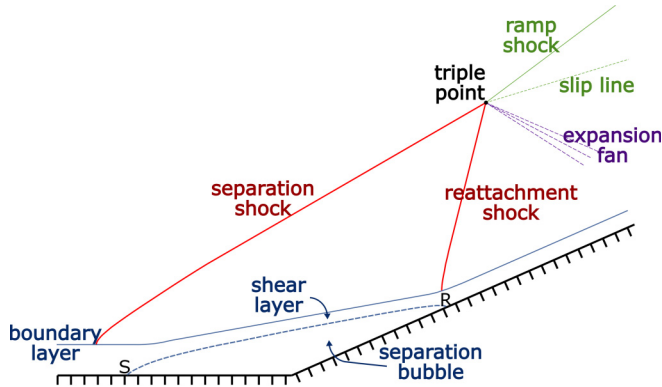
FIG. 1. Canonical SBLI.

When the shock to be traversed is sufficiently strong, the boundary layer can become separated from the wall. Figure 1 depicts an illustration of such a canonical SBLI, with the separation and reattachment points denoted by the letters S and R, respectively. The flow is decelerated to stagnation and reversal. The result is similar whether the SBLI was caused by an incident shock or a compression corner, as long as the pressure rise is the same. Above the separation bubble, a shear layer exists where viscous effects from the high-speed freestream accelerate the flow along the separation streamline until it is decelerated by reattachment. The pressure at the wall upstream of the separation point increases rapidly, followed by a decrease in slope or a plateau of the wall pressure inside the separation bubble. The pressure rises at a higher rate again at reattachment [2].

B. Hypersonic transitional separation

Initial supersonic and hypersonic research focused on the factors that affected the size and extent of the separation bubble. Becker and Korycinski [3] were the first to focus on the effects of transition on SBLI separation. They performed a study on ogive-cylinder-flare models with $10°$ or $30°$ flare angles at Mach 6.8 in the Langley 11-inch hypersonic tunnel. Their experiment covered a variety of Reynolds numbers such that transition was located either prior to separation, above the separation bubble, or after reattachment. They observed that the separation point moved upstream with increasing Reynolds numbers when the transition point was downstream of reattachment. However, as transition moved forward, this trend reversed, and the separation point moved downstream with increasing Reynolds number. Once transition was upstream of the separation point, the boundary layer was turbulent at the corner and only minimal separation was seen. Additionally, Becker and Korycinski saw rapid fluctuation in the separation point location when the transition point was nearby. Chapman, Kuehn, and Larson in 1958 conducted an experimental and theoretical study of separated flows at NACA [4]. They were the first to look at "free interaction" of the boundary layer with the external flow in supersonic cases as they relate to separation. They also compared the bubble properties across a large number of freestream conditions. While they did not specifically study the hypersonic regime, they did cover Mach numbers from 0.4 to 3.6 and a large range of Reynolds numbers. Their work pointed out the Mach number effect on separated laminar boundary layer stability, with higher Mach numbers increasing the stability of a separated laminar mixing layer.

The study of unsteadiness related to supersonic separated flow did not begin in earnest until the early 1980s. Dolling and Murphy conducted experimental research on wall pressure fluctuations in two-dimensional turbulent SBLIs in 1982 [5]. Their measurements found significant pressure fluctuations throughout the flowfield, although they were especially present at the point of separation due to unsteadiness in the shock causing streamwise oscillations of the shock itself.

In 2003 Vandomme *et al.* at ONERA reported an experimental and numerical study on transitional SBLIs at Mach 5 [6]. They tested a hollow cylinder-flare model and compared the experimental results to numerical calculations. To distinguish transition as the result of separation from natural unseparated transition, they also used a cylindrical attachment to the base of the model, replacing the flare; from this configuration, they determined that separation does not seem to induce transition on the model at high Reynolds numbers. This conclusion was drawn due to the similar transition locations as determined by heat flux measurements between the model with and without the flare. This work was followed up by Benay *et al.* in 2006 looking at more numerical results to compare with additional experimental data taken at ONERA [7].

Second (Mack) mode fluctuations in particular were the focus of Balakumar *et al.* [8], who performed a numerical study in 2005 on hypersonic boundary layer stability with a compression corner. They simulated the lower surface of the Hyper-X model as well as the experimental conditions it was subject to at the NASA LaRC 20-Inch Mach-6 Wind Tunnel. Their study found that second-mode waves amplified at the rate suggested by linear stability theory in the region prior to separation, then maintained their amplitude over the separated region (without entering the separation bubble), and finally proceeded to amplify after reattachment. In the region of separation, several unstable modes were seen, and the second mode was found to have a lower frequency than in the regions around it. They concluded that transition due to the second mode was unlikely to occur before the downstream end of the separation bubble. Similar second-mode neutral stability over a separation bubble has been observed by Benitez *et al.* [9,10] and Butler and Laurence [11,12].

A review of instabilities associated with laminar boundary-layer separation in low-speed flows was written by Dovgal *et al.* [13]. While not covering high-speed separation, the review did include multiple studies that noted that traveling instabilities generated in or amplified by the shear layer over a separation bubble were significant for transition. A linear stability analysis by Sandham and Reynolds determined that oblique modes may be dominant for high Mach-number shear-layer flows [14]. Several hypersonic studies have been conducted to determine if such a shear-layer instability is present above Mach 5. Initial work was conducted by McKiernan in the Boeing/AFOSR Mach-6 Quiet Tunnel (BAM6QT) at Purdue University [15–18]. A variation on the Oberkampf cone-with-slice-and-flap model [19] with a sharp $7°$ half-angle cone as the base shape and flaps with deflection angles of $10°$, $20°$, and $30°$ as the modular compression corner was run at a variety of unit Reynolds numbers. The second mode was damped on the slice, but lower frequency absolute (as opposed to convective) instabilities developed in the same region [17]; this result is similar to what was observed on a hollow cylinder-flare model made by Leinemann *et al.* [20]. No frequency peaks were seen downstream of reattachment on the Oberkampf geometry, where broadband increase of the power spectra of the surface pressure fluctuations occurred as transition happened. However, with the introduction of artificial disturbances to the boundary layer upstream of the separation, a convective instability was observed in the reattached boundary layer, which increased in frequency as it traversed downstream [17].

Around the same time, experimental studies at Sandia National Laboratories were also being conducted on the Oberkampf geometry under Mach 5 and 8 flow by Pandey *et al.* [21]. They observed fluctuations in the shear layer via schlieren imagery and measured high-frequency peaks in surface pressure spectra; they speculated that these pressure peaks were related to the shear-layer unsteadiness. They found that the surface pressure fluctuations decreased in frequency moving downstream, which differs from McKiernan's artificial disturbance results. In 2022 they performed a more detailed experiment at Mach 8, which included focused laser differential interferometry (FLDI) data, as well as higher-speed schlieren to better measure the off-surface shear-layer fluctuations [22]. These results confirmed the earlier surface-pressure measurements, where coherent fluctuations measured in the shear layer decreased in peak frequency moving downstream. These shear-layer fluctuations coalesced as a broad "flapping" motion, which radiated shocklets towards the freestream and acoustic waves towards the surface through the separation bubble.

Benitez *et al.* [9] were the first to measure a natural, convective shear-layer instability in axisymmetric hypersonic flow. By testing a cone-cylinder-flare geometry in the BAM6QT, they

observed both second-mode waves and another convective instability downstream of reattachment under quiet flow without perturbation. The other instability was determined to be related to the separation bubble and first appears in FLDI measurements of the shear layer just upstream of reattachment. This instability behaved similarly to the artificial waves measured by McKiernan, with peak frequency increasing moving downstream. Butler and Laurence [12] found a similar instability the next year in the University of Maryland HyperTERP hypersonic shock tunnel. They observed a shear layer instability around 75 kHz upstream of reattachment using high-speed calibrated schlieren. A further study conducted in 2022 studied the effect of compression angle on boundary-layer and shear-layer instabilities [23]. As the flare angle increased, the dominant instability shifted from the second mode to the lower-frequency shear-layer instability.

In 2020 a detailed computational study by Lugrin *et al.* [24] examined a transitional SBLI caused by a $15°$ axisymmetric ramp at Mach 5. They utilized spectral proper orthogonal decomposition (SPOD) to investigate the transition mechanism and determined that it resulted from the linear amplification of oblique modes. Nonlinear interaction between these modes created the streamwise striations that are often observed in experiments [25,26]. Lugrin *et al.* [27] in 2022 conducted a high-fidelity simulation of a similar scenario based on experiments conducted by Benay *et al.* [7]. They found two modes appeared with the separation bubble: a steady mode near reattachment that is associated with streamwise vortices and an unsteady mode that likely causes the bubble to "breathe" with movement of the separation and reattachment points. These results are comparable to a computational study by Cao *et al.* [28], which found unsteady modes identified by dynamic mode decomposition in agreement with a global stability analysis for a compression ramp at Mach 7.7. Later work by Cao *et al.* [29] found that an intrinsic instability lead to transition to turbulence in a direct numerical simulation (DNS) without the introduction of any external disturbances.

Also in 2022, Lugrin *et al.* [30] described results from experiments on a hollow cylinder-flare model with a sharp leading edge at the R2Ch blowdown tunnel at ONERA. Using heat transfer measurements, they found clear streaks under the reattached boundary layer at various wave numbers, similar to prior results by Ginoux [25] and Leinemann *et al.* [20] on the same type of geometry. They also conducted an SPOD analysis on high-speed schlieren imagery, finding oblique shear layer modes to be dominant over the separated region. Their work involved a transitional separation bubble, which was laminar at separation but transitional at reattachment, studied at three different freestream unit Reynolds numbers.

Recently Paredes *et al.* [31] conducted a computational investigation of convective and global boundary-layer instabilities over a sharp-cylinder-flare model at Mach 6. Their study involved a $10°$ flare and utilized wall-pressure sensors at the BAM6QT to measure the distinct lobes within the disturbance amplification spectra. They reported that oblique Mack's first-mode waves, which begin to amplify over the cone, continue to grow along the separated shear layer. In a separate study, Dwivedi *et al.* [32] investigated a globally stable double-wedge flow at Mach 5 using weakly-nonlinear input-output analysis and direct numerical simulations. They discussed that the amplification of oblique waves was due to shear stress fluctuation caused by streamline curvature, highlighting it as the physical mechanism for the amplification of these waves.

The present study extends the work by Benitez *et al.* [9,10], Butler and Laurence [11,12], Benitez *et al.* [33], Benitez [34], and Paredes *et al.* [31] by utilizing an axisymmetric cone-cylinder-flare configuration to look at hypersonic instabilities and separation in a quiet environment. Such a low-disturbance environment allows for measurements made on a large range of Reynolds numbers while maintaining laminar separation and reattachment. It also provides freestream noise conditions that are more closely related to what might be experienced in flight [35–37]. This work includes experimental testing in the BAM6QT with FLDI density gradient fluctuation measurements, PCB and Kulite surface pressure measurements, infrared thermography heat-transfer measurements, and schlieren imagery. The paper presents evidence of the source of the shear-layer instability by contrasting the measurements with a no-separation case that has a smaller flare angle. Additional computational analysis has been conducted for both the separation and no-separation cases, with results comparing computed off-surface fluctuations directly with FLDI measurements. Evidence
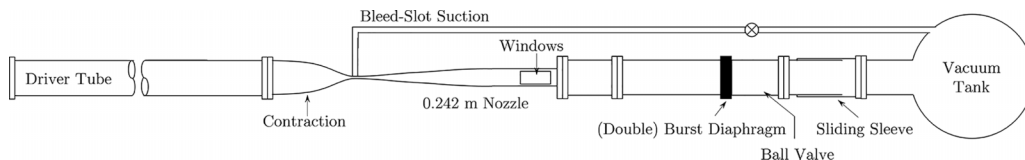
FIG. 2. BAM6QT schematic.

of a lack of large-scale bubble fluctuations under quiet flow is shown, which contrasts with the usual fluctuations measured under conventional noise for such hypersonic laminar separations. Experimental measurements of nonlinear phase locking between the shear-layer instability and the second mode are also provided. Finally, an analysis of the resulting disturbance packets from upstream plasma perturbation is presented.

II. EXPERIMENTAL SETUP

A. Boeing/AFOSR Mach-6 quiet tunnel (BAM6QT)

Hypersonic experiments were conducted in the Boeing/AFOSR Mach-6 Quiet Tunnel (BAM6QT) at Purdue University. The BAM6QT is a Ludwieg tube that is capable of being run with noisy or quiet flow with run times of up to 6 s. It consists of a 40.8-m driver tube connected to a converging-diverging nozzle that exhausts into a 113 m^3 vacuum tank. The test section is located in the downstream end of the diverging section of the nozzle and includes optical access with contoured plexiglass windows. A diagram of the tunnel can be found in Fig. 2.

To obtain quiet flow, a combination of several features are implemented to reduce disturbances and keep the boundary layer on the nozzle laminar. The nozzle of the BAM6QT is polished to a mirror finish to reduce the presence of roughness on the surface. Additionally, the nozzle itself is long such that the radius of curvature in the streamwise direction is large, reducing amplification of the Görtler instability. Air travels through a particle filter before entering the driver tube to remove most particles such that the air is similar to that in a clean room. Finally, bleed slots are located at the throat of the nozzle. These slots use suction to remove the boundary layer from the nozzle so it begins again at the throat, thereby removing any disturbances that might convect from the contraction section. Together, these features allow the tunnel to operate with very low freestream noise levels (less than 0.02%). However, at high enough Reynolds numbers the flow will still be noisy. For these experiments, the tunnel was capable of operating quietly at up to a unit Reynolds number of around 12×10^6/m with the exception of two entries. Those entries had a maximum quiet unit Reynolds number of approximately 10×10^6/m.

B. Models

Two variants of a sharp cone-cylinder-flare geometry were studied: one with a 3.5° flare, and the other with a 10° flare. The 3.5° model was designed to introduce an axisymmetric compression to the flow but not cause boundary-layer separation. The 10° flare was selected to create an axisymmetric separation bubble through SBLIs, with the angle chosen through computational analysis [38].

Both versions are made of three components, of which they share the two upstream-most parts: a sharp (0.1 mm radius) stainless steel nose tip and an aluminum cone cylinder. The cone has a 5° half-angle and is 0.399 m long. The third component is a PEEK cylinder flare. The complete cylinder is 0.127 m long for both variants. The flare is 0.239 m long for the 3.5° angle, while it is only 0.122 m long for the 10° flare due to tunnel blockage constraints. Figure 3 contains an illustration of the two models with dimensions for reference.

A second version of the aluminum cone-cylinder section was made for artificial disturbance tests with the 10° flare. This version included a pair of electrodes located 0.387 m downstream of the nose tip, near the downstream end of the cone just before the cylinder. The gap between the electrodes was

(a) 3.5° flare model illustration
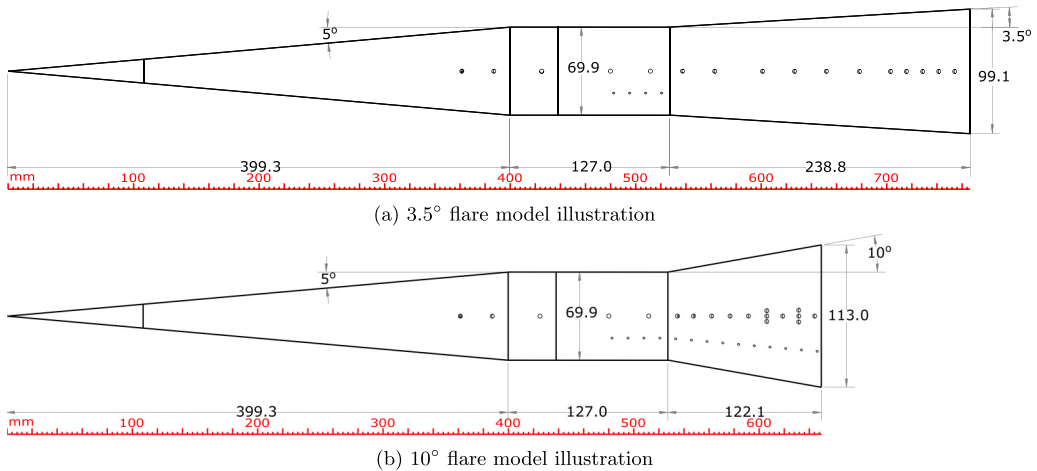

(b) 10° flare model illustration

FIG. 3. Model illustrations with select dimensions in mm.

set at 1.78 mm, which was designed to cause an electric discharge in air based on Paschen's law. This perturber design is based on those used by Casper [39] and McKiernan [17,18]. Figure 4 displays photographs of the models, with the 3.5° model including the original cone-cylinder section and the 10° model with the second version with electrodes.

C. Instrumentation

Surface-pressure fluctuations were measured using PCB132B38 sensors manufactured by PCB Piezotronics. These sensors are high-pass filtered above 11 kHz and have a high-frequency response limit of 1 MHz. Therefore, their output was always sampled at 2 MHz with either Tektronix oscilloscopes or an HBM data acquisition system. The PCB sensors have a stated resolution of 7 Pa with a rise time of less than 3 μs [40]. The PCB factory calibrations provide a single number to convert voltages to pressure fluctuations; this value was used to scale the voltages to pressure
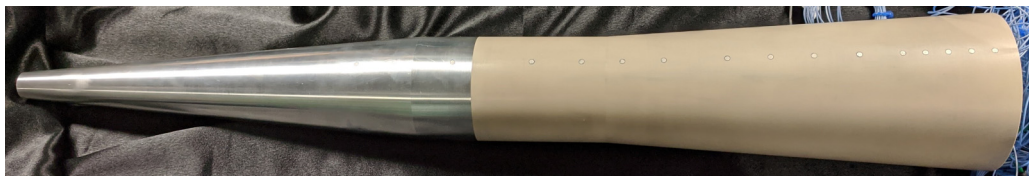
(a) 3.5° flare model

(b) 10° flare model

FIG. 4. Cone-cylinder-flare models used for experiments, with nose tips removed. The 10° model is shown with electrodes for plasma perturbation on the cone section.

measurements. Additional surface-pressure measurements were made with Kulite XCE-062-15A sensors, but due to the similarity in their results only the PCB measurements are shown here.

An InfraTec ImageIR camera was used to surface temperature of the PEEK models, which was then used to compute surface heat flux. IR thermography provides less noisy temperature measurements than temperature-sensitive paint [41] and are not dependent on the quality of the paint job prior to each entry. The InfraTec thermographic software IRBIS 3 was used to control the camera and record the temperature data. The Purdue Infrared Registration ANd Heat Flux App (PIRANHA) developed by Edelman was used to calculate heat flux from these temperature measurements [42].

The heat flux results were computed on a conical mesh applied to the surface of the flare. This allows the three-dimensional results to be viewed on a two-dimensional surface, with the flare unwrapped and stretched onto a rectangular plane with axes of downstream distance and azimuthal angle. The heat flux was used along with the computed unit Reynolds number and temperature values to normalize it along that surface. Equation (1) shows the computation used to determine the Stanton number (St):

$$St = \frac{q''}{\mu \mathrm{Re} c_p (T_0 - T_w)}.$$ (1)

In this equation, q'' is the heat flux determined by PIRANHA, and μ is the fluid viscosity calculated using Sutherland's law without the low-temperature correction. Re is the freestream unit Reynolds number, and T_0 is the stagnation temperature. T_w is the wall temperature, which was generally around 303 K based on the average measured surface temperature, and c_p is the specific heat, assumed to be 1009 J/(kg-K).

A focused laser differential interferometer (FLDI) was utilized to make off-the-surface measurements of density fluctuations for the separated flow. Initially designed by Smeets and George in the 1970s [43–47], the technique was first used for hypersonic instability measurements in the early 2010s [48–50]. An FLDI is a common-path interferometer that measures the phase change between the two beams, which occurs due to the linear relationship between a fluid's refractive index and its density [51]. This relationship is described in Eq. (2a), where K is the Gladstone-Dale constant, ρ is the density of the fluid, and n is its index of refraction. From the measured phase change ($\Delta\phi$) and known wavelength of the laser (λ_0), an optical path difference (Δs) can be computed [Eq. (2b)]. The optical path difference, along with an integration length (L) and the Gladstone-Dale constant, can be converted to an estimate of the density gradient fluctuation [Eq. (2c)]:

$$K\rho = n - 1,$$ (2a)

$$\Delta\phi = \frac{2\pi}{\lambda_0}\Delta s,$$ (2b)

$$\Delta s = LK\Delta\rho.$$ (2c)

While not as accurate a methodology as utilizing transfer functions [52], this method has been shown to provide density gradient measurements with an error less than 20% [53]. The particular FLDI apparatus used for these measurements used a Research Electro-Optics (REO) 633 nm He-Ne laser system with 2 arcminute Wollaston prisms, which resulted in a beam spacing of 103 μm. An integration length of 65 mm was used when calibrating the data, based on bench tests of the FLDI aparatus with a narrow-diameter jet. The apparatus is described in more detail in Benitez *et al.* [54–56].

Finally, schlieren images were taken of the separation bubble with the 10° flare. A Newport xenon light source was used with 4-inch parabolic mirrors. A Photron SA-Z high-speed camera was used to record the images, with a frame rate of 20 000 frames per second and a shutter speed of 1/4 032 000 seconds.
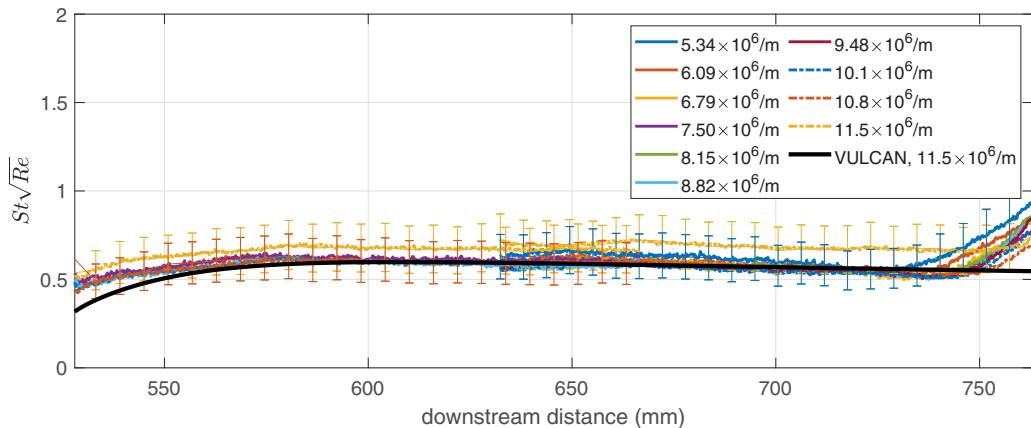
FIG. 5. Normalized heat flux along 3.5° flare under quiet flow at various unit Reynolds numbers. Due to the restricted optical access, two runs had to be made at a given Re value to encompass the entire flare. The compression corner is located at 526 mm, just to the left of the first vertical axis, while the downstream edge of the model is at 765 mm. Here 20% error bars are included for the largest and smallest unit Reynolds number cases.

D. Computational setup

Computations of this geometry were conducted with the second-order finite-volume Navier-Stokes code VULCAN-CFD to compute the laminar flow over the 3.5° and 10° models and with a hybrid methodology of the parabolized stability equations (PSEs) and the harmonic linearized Navier-Stokes equations (HLNSEs) to calculate the linear amplification of convective instabilities. Similarly to Paredes *et al.* [31], the laminar flow solutions were calculated with a grid of 3601×1201 points along the streamwise and wall-normal directions, with an isothermal wall of 300 K. For the PSE and HLNSE calculations, sixth-order finite-difference schemes were utilized across a nonuniform grid along the wall-normal direction. There were 201 points in the wall-normal direction, with points clustered near the wall. Second-order backward differentiation was used to integrate the discretized PSE along the streamwise direction. The HLNSEs were discretized with 2001 points in the streamwise direction. At the wall, no-slip isothermal boundary conditions ($\hat{u} = \hat{v} = \hat{w} = \hat{T} = 0$) were set, while at the far-field boundary, the amplitude functions were forced to decay via the Dirichlet conditions ($\hat{\rho} = \hat{u} = \hat{w} = \hat{T} = 0$). The HLNSE initial conditions were set based on the PSE solution upstream of the cone-cylinder corner.

III. BASELINE CASE WITH NO SEPARATION

To provide a baseline for the effect of a hypersonic axisymmetric compression on boundary-layer instabilities, a 3.5° flare angle was used. This flare angle creates a weakly interacting flow through SBLIs and was selected after a series of computations were completed by Esquieu on various cone-cylinder-flare parameters [38]. With this geometry, no boundary layer separation takes place. Heat flux and surface pressure fluctuation measurements were taken to study the natural instabilities along the surface of the model. All measurements were made at a near-zero (less than 0.1°) angle of attack, and only the natural instabilities were studied. Under the quiet flow, the boundary layer appeared to remain laminar for all test conditions.

Figure 5 provides comparison of the normalized heat flux averaged from slices taken between 80° and 100° in the azimuthal direction along the flare (where 0° corresponds to the azimuthal location of the main sensor array). Due to the smaller size of the window relative to the length of the flare, the heat flux is shown in two parts. In these quiet flow runs, the heat flux is relatively constant across
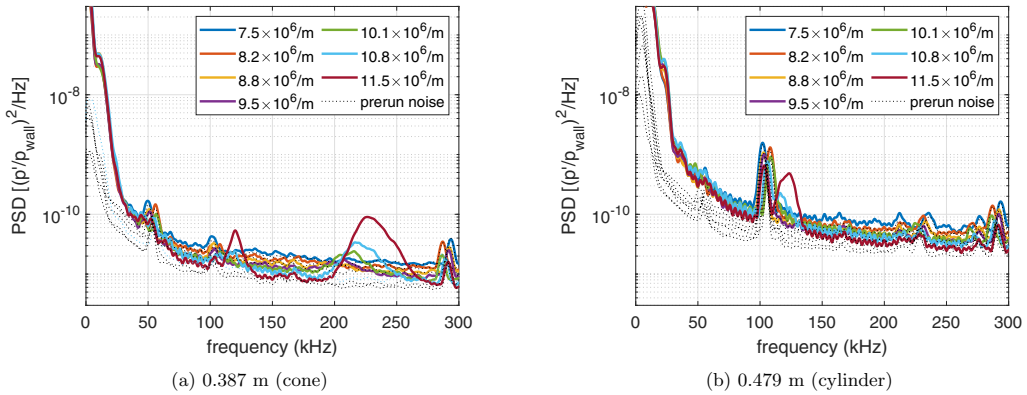
(a) 0.387 m (cone)　　　　　　　　　　(b) 0.479 m (cylinder)

FIG. 6. PCB PSDs along the $5°$ cone and the cylinder at Re between 5.34×10^6 and 11.5×10^6/m in quiet flow.

the surface of the flare, with only slight increases seen towards the downstream edge. In general, heat flux values for all of these runs collapse on top of each other. The computed heat flux is shown in black. It agrees well with the majority of the experimental data.

Around 740 mm downstream of the nose tip, the heat flux values begin to rise for all cases. This rise could potentially mark the onset of transition, although it does not seem to be influenced by unit Reynolds number in terms of location or magnitude. Pressure fluctuation power spectral densities in that region do not show any peak broadening that is indicative of transition [see Fig. 7(b) below]. Due to its downstream location, the heat flux increase could potentially be due to end-of-model conduction effects as well. An additional, although less significant, departure from the computed estimate occurs upstream of 550 mm. While the cause of this mismatch is uncertain, it may be due to a lack of sensitivity in the experimental tests from the low temperature rise in this region. Another possibility is that there are 2D conduction effects occurring; since the streamwise heat flux increases at a greater rate just downstream of the compression corner, the resulting streamwise temperature gradient may be sufficient to drive some streamwise conduction. The computed heat flux does remain within the 20% uncertainty of the experiments for the entire flare with the exception of the downstream edge.

Figure 6 displays some of the PCB pressure power spectral densities (PSDs) at various unit Reynolds numbers along the cone and cylinder, normalized by wall pressure values computed by Esquieu *et al.* [38]. The PCB signals were high-pass filtered at 500 Hz. Second-mode fluctuations are apparent on the cone section between 200 and 300 kHz at unit Reynolds numbers 9.5×10^6/m and above. The second mode is damped as it goes through the expansion along the cylinder. As the unit Reynolds number increases, so does the instability amplitude and peak frequency, as expected for the second mode. The sharper peaks at various frequencies are also present in the prerun voltages and are therefore due to electronic noise.

The fluctuations from the second mode along the flare were found between 100 and 150 kHz, due to the thicker boundary layer along the flare relative to the cone. For the highest unit Reynolds numbers, fluctuations in this band were also measured upstream on the cone and cylinder segments. It may be the case that the second-mode fluctuations were transmitted upstream from the flare section. While the reason for this potential signal contamination is uncertain, it is possible the transmission is through model vibration. The same cone-cylinder model segment is used in the separating experiments, where only the expected second-mode peaks are seen along the cone and cylinder (see Fig. 19 below). The $3.5°$ flare model is significantly longer than the $10°$ one, so if the second mode along the flare is inducing vibrations, they would have a larger effect on the longer model. Model vibrations have been seen at such high frequency on long models in other
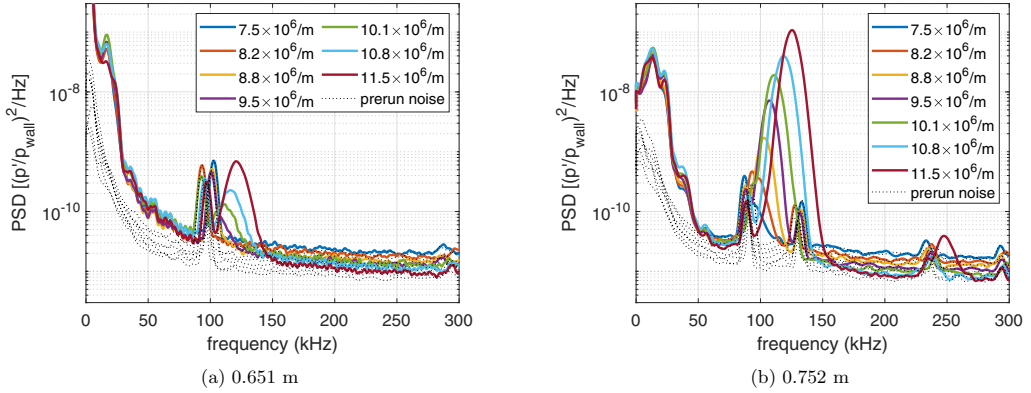
(a) 0.651 m
(b) 0.752 m

FIG. 7. Two PCB PSDs along the 3.5° flare at unit Reynolds numbers between 5.34×10^6 and 11.5×10^6/m in quiet flow.

cases at this facility [57]. Another possibility for the source of these peaks is that the 100–150 kHz fluctuations upstream of the flare are measurements of the first-mode instability. The computations of this geometry do include the first mode in a similar frequency band along the cone and cylinder, although at a low amplitude (see Fig. 21 below). It is conceivable that the first mode is being picked up by the PCB sensors along the cylinder for this model but not the 10° flare model, which has the same cone-cylinder section, because this version does not have a separation bubble along the cylinder.

Figure 7 shows a sample of pressure fluctuation PSDs along the flare. The second mode can be seen amplifying as it moves downstream. The instability peaks increase in amplitude and peak frequency with increasing unit Reynolds number again. As before, sharper spikes present in the prerun data are due to electrical noise.

In general along the flare, other than a second-mode harmonic seen at the highest unit Reynolds number 0.752 m downstream, only one frequency peak is seen at each PCB station (excluding electronic noise spikes). There is a rise in lower-frequency fluctuations, but this is generally broadband as any peaks seem to coincide with the PCB high-pass filtering at 11 kHz. High-amplitude, low-frequency fluctuations are common in PCB spectra and are most likely due to model vibration. The second-mode peaks amplify moving downstream without broadening, implying that the flow remains laminar through the end of the model for all unit Reynolds numbers tested in quiet flow.

Good agreement was found with the computed second-mode peak frequency values (Fig. 8). Because the computational predictions shown in Fig. 8 at $x = 0.752$ m use an initial amplitude set to match the PCB value at an earlier location of $x = 0.651$ m, the peak amplitude evolution also agrees well. Note that at both the earlier station and at $x = 0.752$ m the most amplified disturbance is an oblique mode with the azimuthal wave number $m = 15$. This differs from the usual case for the second-mode instability, which is generally most amplified for $m = 0$. This finding also differs from previous computational results on this geometry [38].

The integrated PCB amplitudes are plotted along with the computed N factors with the same vertical scaling in Fig. 9. The experimental results are shown at each PCB station as a black circle, with the values computed by integrating the measured pressure fluctuations between 100 and 150 kHz. By plotting the data as a function of length Reynolds number (with the reference length equal to the distance between the sensor and the compression corner), they collapse onto roughly a single curve. The computed N factors are plotted as lines, with each color corresponding to a single wave number, m. All of the N factors correspond to the values computed for 120 kHz. Once again, excellent agreement is seen in the amplification rates from the experiment and the computations once the computed N factors rise above the noise floor between $\mathrm{Re}_{x-x_c} = 1 \times 10^6$ and $\mathrm{Re}_{x-x_c} = 1.5 \times 10^6$.
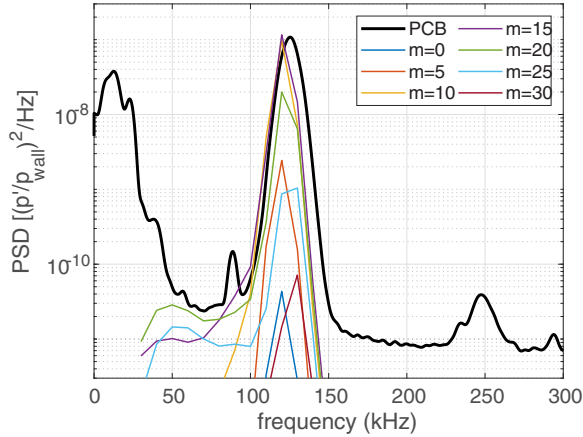
FIG. 8. Measured and computed surface pressure spectra 0.752 m downstream of the nose tip. The thick black line corresponds to the PCB measurement, and the colored lines correspond to the linear amplification of computed planar and oblique waves at different azimuthal wave numbers, m. $Re = 11.5 \times 10^6/m$.

The second mode consists of a traveling wave in the boundary layer. Finding the coherence between two adjacent sensors can determine if an instability at a given frequency is convective. Figure 10 shows the power spectral densities and coherences for the PCBs on the downstream portion of the flare at $Re = 11.5 \times 10^6/m$. The PCB signals were high-pass filtered at 25 kHz before the coherence was calculated. The second mode can be seen in the PSDs for each sensor around 125 kHz, with the farthest downstream PCBs also showing the first harmonic at 250 kHz [Fig. 10(a)]. Narrow peaks present in the prerun spectra are due to electronic noise. The coherence plot [Fig. 10(b)] shows values near unity in the same band as the second mode, as well as moderately high coherence for the first harmonic. Due to the high coherence values for the sensors located along a streamwise ray, the instability is likely to be convective, as expected for the second mode.

Figure 11 plots time series data from consecutive PCB sensors, highlighting wave packets of the second mode as they amplify and convect downstream. Several second-mode wave packets can be seen with very low amplitude at 0.677 m from the nose tip. These packets shift later in time as
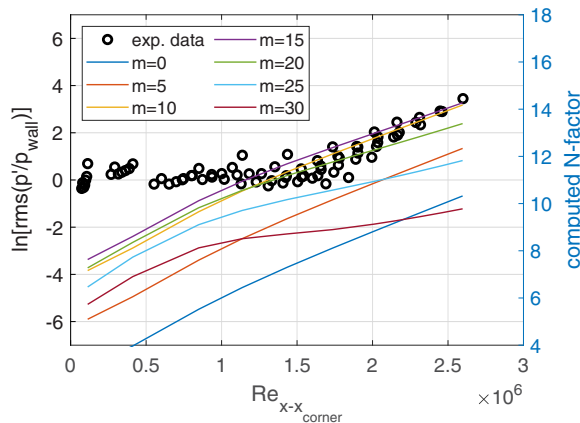

FIG. 9. Measured PCB integrated fluctuation amplitudes compared to computed surface pressure N factors. The measured fluctuations are integrated between 100 and 150 kHz, while the computed N factors were at 120 kHz.
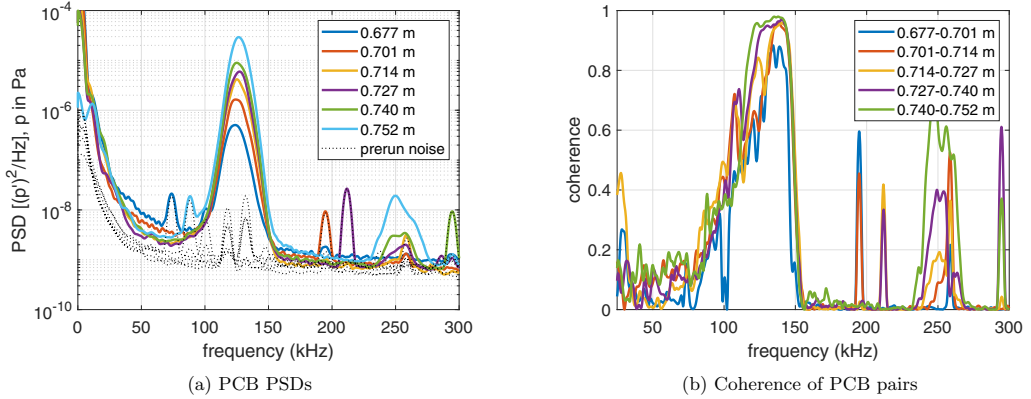
FIG. 10. Power spectral densities and coherence between PCB sensors, Re $= 11.5 \times 10^6$/m. High coherence values for all pairs in the second-mode band (100–150 kHz) signify a convective instability.

they move downstream, increasing in amplitude at each successive sensor. By cross-correlating the signals, a disturbance velocity of the wave packets can be determined [see Fig. 12(a)]. The velocity is found by fitting a line to the plot of lag at maximum cross-correlation versus downstream distance [Fig. 12(b)]. The second-mode waves convect with a speed of approximately 711 m/s (about 86% of the shock-layer velocity). The second mode disturbance speed is very close to the phase velocity of a slow acoustic wave, $c = (1 - 1/M)U_\infty$, where $c = 0.83U_\infty$ for $M = 6$ (or $c = 0.80U_\infty$ for $M = 5$, which may be closer to the true value along the flare) [58]. The frequency of the waves is around 125 kHz, as determined by counting the number of cycles in a given time period. This frequency also corresponds to the peak of the pressure power spectra at this unit Reynolds number (11.5×10^6/m).

In summary, an axisymmetric compression without separation has only the second-mode instability present in the surface pressure spectra. Though damped through the expansion between the cone and cylinder, it returns along the flare and resumes amplifying as it propagates downstream.
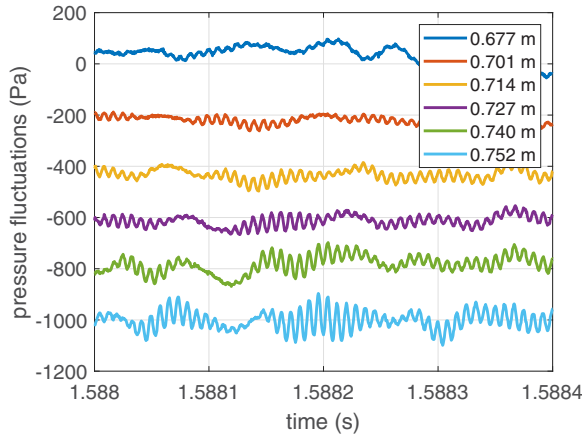

FIG. 11. Waterfall plot showing the amplification of second-mode wave packets as they convect downstream. The PCB pressures are vertically offset for clarity. Re $= 11.5 \times 10^6$/m.
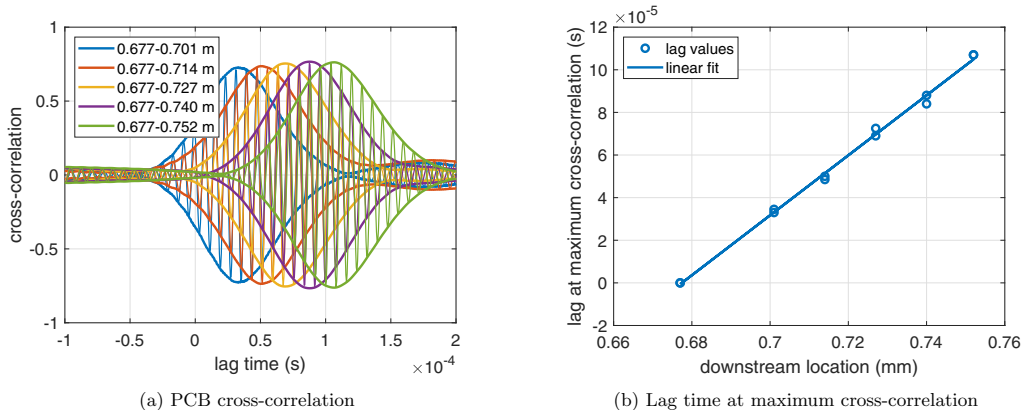
(a) PCB cross-correlation

(b) Lag time at maximum cross-correlation

FIG. 12. Cross-correlation values between PCB sensors along the flare and their lag time at maximum cross-correlation. Re $= 11.5 \times 10^6$/m.

IV. RESULTS FOR SEPARATED FLOW

A $10°$ flare angle was used to model an axisymmetric compression corner that creates a separation bubble through an SBLI. Heat flux, surface pressure fluctuation, schlieren, and FLDI measurements were made for this geometry. Most measurements were made at a near-zero angle of attack, although small angles of attack were also studied (see Benitez *et al.* [33] for nonzero angle of attack results). In addition to the natural instabilities of the flow, artificial perturbations were introduced in the boundary layer upstream of the separation bubble to study how the generated wave packets evolve moving through the shear and boundary layers. As with the nonseparating case, with quiet flow the boundary layer appeared to remain laminar for all test conditions, even downstream of reattachment.

A. Bubble geometry

To understand the instabilities in the shear layer and reattached boundary layer, it is important to know where along the flare reattachment takes place. This location was determined with schlieren images and is supported by heat-transfer measurements at the wall.

Schlieren images were taken of the cylinder-flare section of the model. Figure 13 shows a composite image taken from six runs at Re $= 11.7 \times 10^6$/m under quiet flow. In this figure the shear layer and reattached boundary layer are seen as white lines off the surface of the model. At
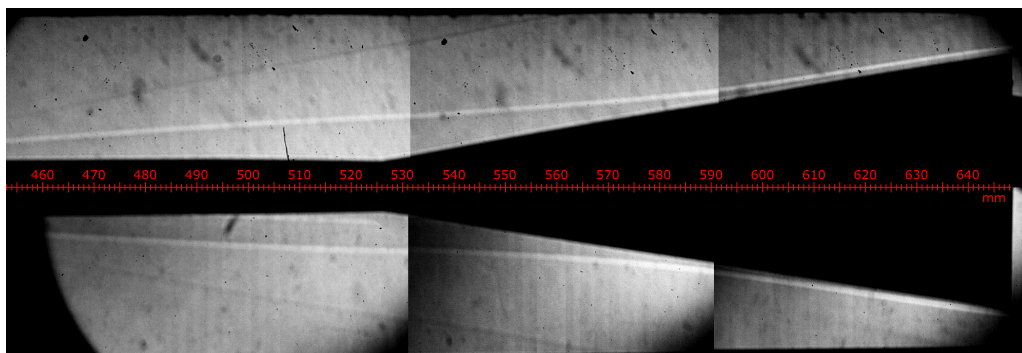

FIG. 13. Composite of six schlieren images at Re $= 11.7 \times 10^6$/m. Flow is from left to right. Dimensions are in mm from the sharp nose tip.
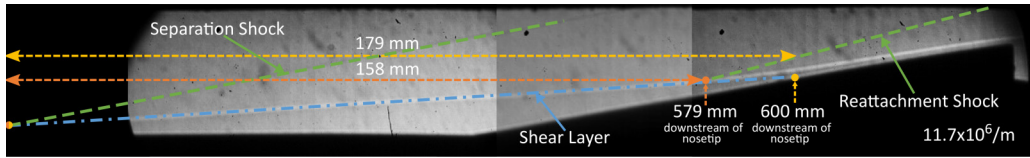
FIG. 14. Illustration of bubble size estimation methods overlaid on composite schlieren image at Re = 11.7×10^6/m. The orange dots represent the estimated separation and reattachment points found by extrapolating the separation and reattachment shocks to the shear layer, and the yellow dots represent those found by extrapolating the shear layer to the model surface. The separation point for both methods is in approximately the same location for this case. Flow is from left to right.

the corner, the shear layer is between 7.6 and 8.2 mm away from the wall when looking at the lower or upper surface, respectively (a less than 8% variation). Note that the model was shifted upstream between runs to obtain the appropriate view through the windows. This shift may have very slightly altered the model's angle of attack, causing the difference in shear layer heights at the edges for this composite image. The separation shocks are clearly visible, while faint smudges can be seen in the farthest downstream images corresponding to the reattachment shocks.

The size of the bubble can only be indirectly approximated from the schlieren. There are several methods for doing this. Schaefer and Ferguson [59] used extrapolation of the shear layer to the model surface to determine separation and reattachment. With this method, the bubble at Re = 11.7×10^6/m would be 179 mm long, reattaching 600 mm downstream of the nose tip. Ginoux [25] used extrapolation of the separation and reattachment shocks to estimate separation extent. This method results in a 158-mm-long bubble that reattaches 579 mm downstream of the nose tip; this location appears to coincide with a change in slope of the shear layer. Most likely, reattachment is somewhere between those two values. For both approximations, the boundary layer separates from the model surface about 105 mm upstream of the cylinder-flare corner, which is downstream of the cone-cylinder junction. Figure 14 provides an illustration of these two estimation methods.

Schlieren images from two different unit Reynolds numbers are displayed in Fig. 15. At the corner, the shear layer is 8.2 and 5.8 mm off-surface at the higher and lower unit Reynolds numbers, respectively. The lower unit Reynolds number case has a lower contrast image due to the lower density gradients in the flow, so the separation and reattachment shocks are not visible. However, since the shear layer height is lower, the bubble is most likely smaller in the 2.55×10^6/m case. Using the shear layer extrapolation estimate of bubble size, the separation bubble is approximately
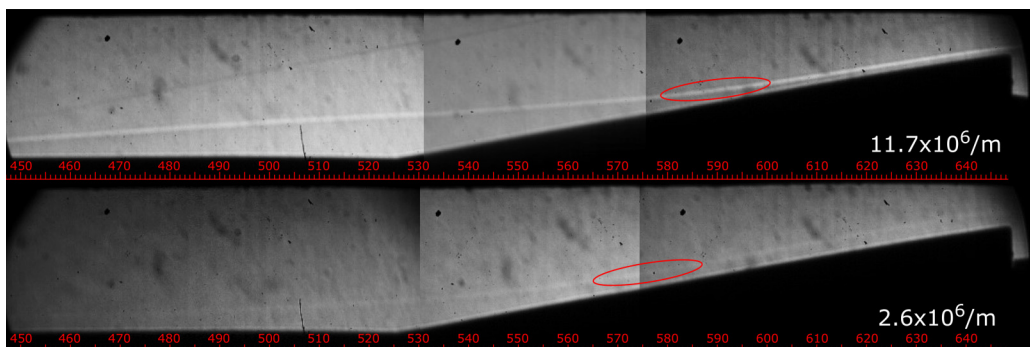

FIG. 15. Composite schlieren images at Re = 11.7×10^6/m and Re = 2.55×10^6/m highlighting variation in bubble size at different unit Reynolds numbers. Estimated reattachment positions are circled in red. Flow is from left to right.

(a) Conventional noise, $Re = 2.3 \times 10^6$/m
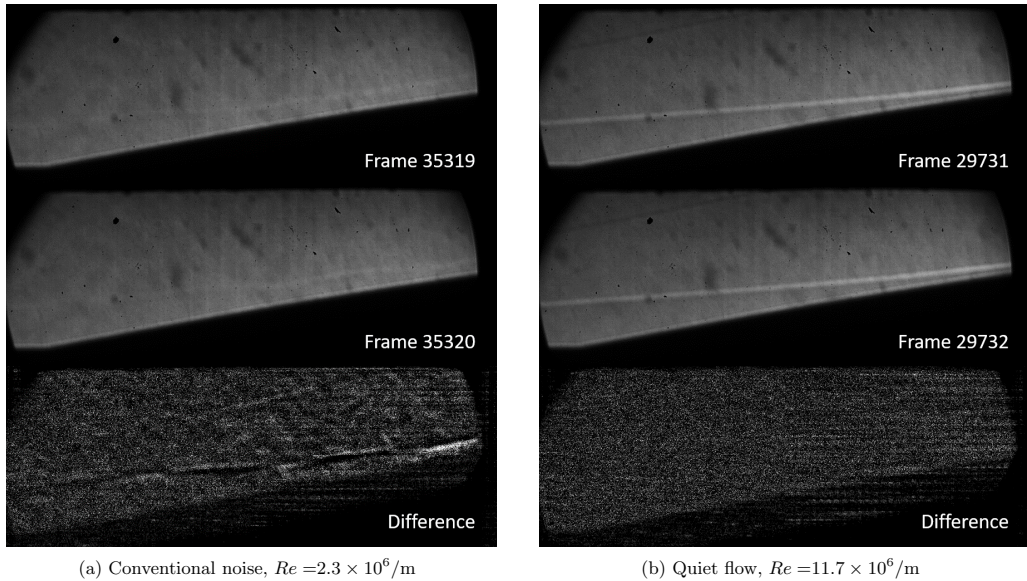
(b) Quiet flow, $Re = 11.7 \times 10^6$/m

FIG. 16. Consecutive frame differences for schlieren images taken at 20 000 frames per second under both conventional noise and quiet flow. The shear layer is laminar for both cases. Flow is from left to right.

136 mm long, reattaching around 585 mm downstream of the nose tip. The trend of increasing bubble size with increasing unit Reynolds number is a laminar trend that has been seen in previous experiments with supersonic and hypersonic laminar bubbles [3,60].

Schlieren images of the separation bubble taken at 20 000 frames per second allow for the low-frequency unsteadiness of the bubble to be observed. However, under quiet flow, it was determined that the bubble was remarkably steady, with no "breathing" detectable. This differed from runs made under conventional noise in the same tunnel, where significant shear-layer fluctuations were observed. For each quiet-flow run, schlieren images revealed that, once established over the course of about 10 ms, the bubble does not fluctuate in size or position during the steady portion of the flow. Noisy runs, however, exhibit continuous shear-layer motion, even when the shear layer was laminar. Figure 16 displays an example of this difference taken from one conventional-noise run and one quiet-flow run. Taking the difference between two consecutive frames reveals shear layer fluctuations for the noisy case but only white noise for the quiet one. A clearer example of the difference in bubble fluctuations between quiet and noisy flow can be seen in the Supplemental movie [64], which depicts 0.05 seconds of flow at a variety of unit Reynolds numbers collected at 20 000 frames per second. Both unit Reynolds numbers for the quiet flow videos and the lowest unit Reynolds numbers noisy flow case represent laminar bubbles, while the other two noisy runs were transitional. In the quiet-flow cases, the bubble appears to not move at all, while in all of the noisy videos there are significant shear-layer fluctuations.

Heat-flux measurements using IR thermography were made along the flare section for a range of unit Reynolds numbers under quiet flow. A sample of the normalized results can be seen in Fig. 17. In these images the flare has been unrolled and stretched to fit a square two-dimensional surface. In general, the heat flux increases along the extent of the flare, with a location of rapid increase that most likely signifies reattachment. Streamwise streaks, which have been seen in other studies, are not apparent. It was later determined that this particular set of runs had a very small nonzero angle of attack (approximately $0.15°$); when precisely at $0.0°$ streamwise streaks can be observed [33]. Note that apparent streaks in Fig. 17(a) are from the pixels from the original image and not a physical phenomenon of the flow. Moving downstream along the flare, the width of the model increases for
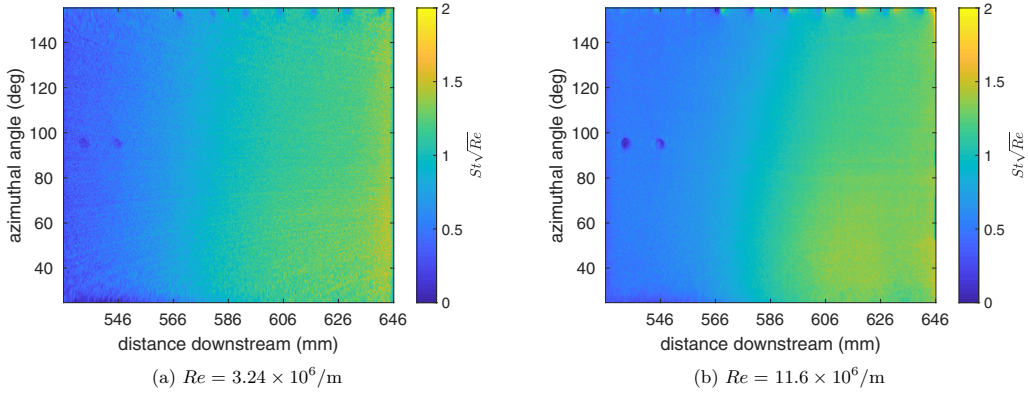
(a) $Re = 3.24 \times 10^6/m$ (b) $Re = 11.6 \times 10^6/m$

FIG. 17. Normalized heat flux images on the unrolled $10°$ flare. Flow is from left to right.

a given azimuthal width, resulting in an increase in the number of pixels, creating the curves seen in the image. These curves are not apparent in Fig. 17(b) due to the higher signal-to-noise ratio from the higher freestream unit Reynolds number.

The unit Reynolds number does not appear to have an effect on the normalized heat flux. Qualitatively, the results are similar in Figs. 17(a) and 17(b). Both cases experience an increase in heat flux near the same location, which most likely means the reattachment point does not vary significantly with unit Reynolds number. In general, the heat flux slowly increased moving downstream along the flare until it reached a steady value around 610 mm. The slight (approximately $-0.15°$) angle of attack for the quiet flow cases is the cause of the asymmetry in the images. The row of dots around $150°$ are Kulite sensors.

Figure 18 plots normalized heat flux as a function of distance downstream, averaged from two slices of the data (located above and below the PCB sensors that can be seen in Fig. 17 at about $90°$). This plot provides a more quantitative view of what is hinted at in the previous figures. The compression corner is at the start of the horizontal axis. The results are laminar and most likely have reattachment points at similar locations (somewhere between 565 and 600 mm downstream
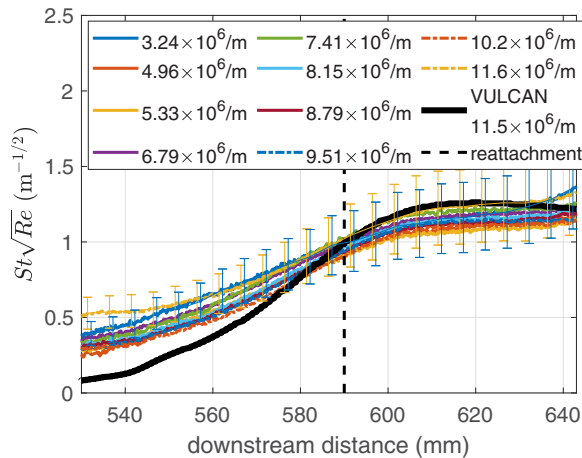

FIG. 18. Normalized heat flux for Re between 3.24×10^6 and $11.6 \times 10^6/m$. The compression corner is at the left edge (526 mm downstream), and reattachment is estimated to be between 579 and 600 mm downstream (the black dashed line represents the center of this range).
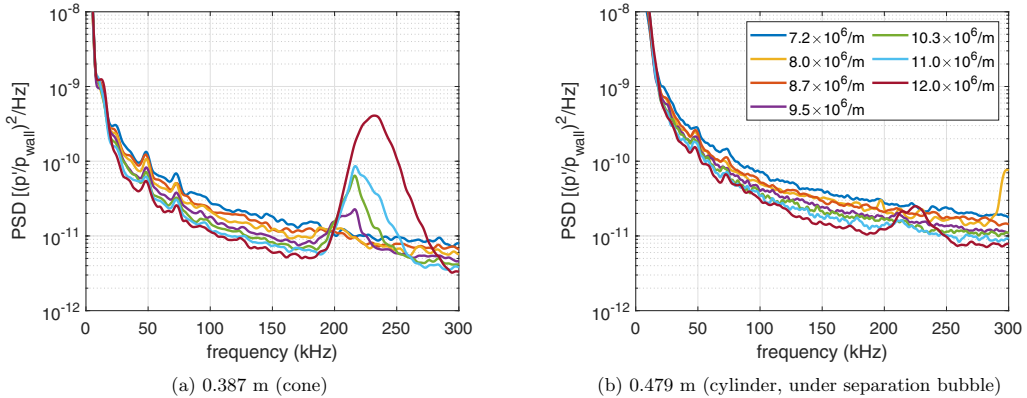
FIG. 19. PCB PSDs along the 5° cone and the cylinder at unit Reynolds numbers between 6.58×10^6 and 12.0×10^6/m. Legend applies to both figures.

of the nose tip across the Re sweep) and so therefore have heat flux profiles which collapse with this normalization. Note that the heat flux profiles appear to begin rising prior to 565 mm, have an inflection point around 580 mm downstream of the nose tip, and reach a plateau by 600 mm, the same axial locations that reattachment is estimated to be between from the schlieren images. The mean-flow computational results from VULCAN-CFD are also plotted. The computed heat flux showed excellent agreement with the experimental measurements downstream of reattachment, although underestimated the values under the bubble. A similar underestimation of the heat flux under the bubble occurred when using a different code, DPLR, to compute the base flow as well [34]. Unfortunately, the cause of this underestimation is currently uncertain, although it may be related to a lack of experimental sensitively to accurately measure such low heat flux values. Alternatively, another possibility is that 2D conduction effects, due to the relatively strong streamwise temperature gradient in this region, are present in the experiment but not the computations.

B. Natural instabilities

PCB and Kulite sensors were used to measure surface pressure fluctuations along the cone, cylinder, and flare sections of the model, while FLDI was used for density gradient fluctuation measurements above the flare. The PCB and Kulite results were similar, so only PCB spectra are displayed here. For the Kulite measurements, see Benitez [34]. The results in this section are for the natural (unperturbed) disturbances measured on the cone-cylinder-flare model at zero degrees angle of attack.

Figure 19 shows the power spectral densities for surface pressure fluctuations along the cone and cylinder across a range of freestream unit Reynolds numbers. Along the cone [Fig. 19(a)], one frequency peak corresponding to the second mode can be seen between 200 and 300 kHz. This peak increases in both amplitude and frequency with increasing unit Reynolds number. On the cylinder under the separation bubble, no visible peaks can be seen over the noise floor except at the highest unit Reynolds number. The second mode is not gone for this section, however; it traverses downstream through the shear layer off the surface of the model.

PSDs of the surface pressure fluctuations along the flare are shown in Fig. 20. Reattachment occurs between 0.58 and 0.60 m downstream. The second mode is visible once again, here between 170 and 290 kHz, with the peak amplitude and frequency increasing with increasing freestream unit Reynolds number. The second-mode peak frequency is higher for this case than for the 3.5° flare due to the thinner boundary layer along the flare downstream of reattachment. The peak amplitude also increases moving downstream, while the peak frequency remains the same in the streamwise direction due to the boundary layer maintaining a relatively constant thickness. A second frequency
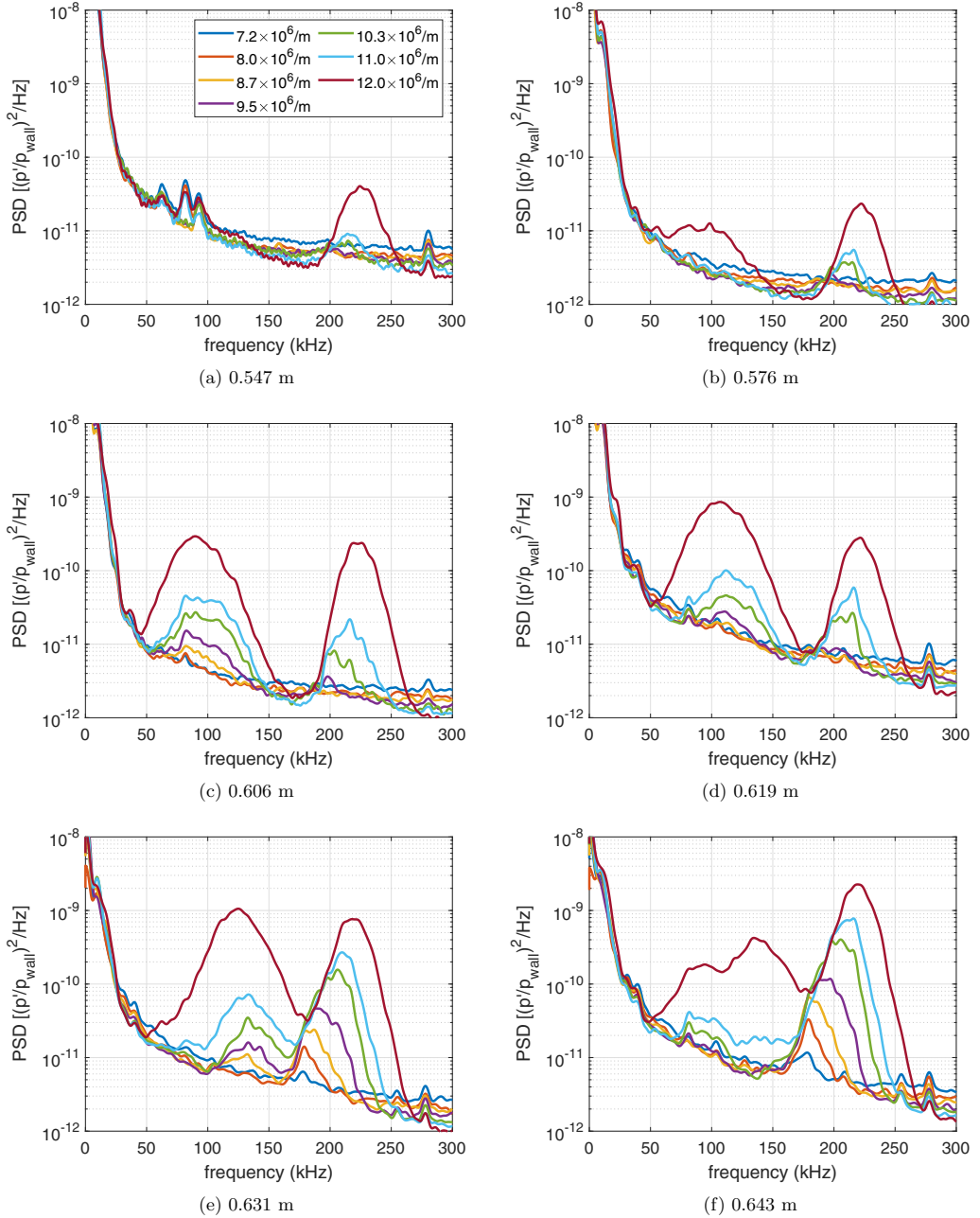
FIG. 20. PCB PSDs along the $10°$ flare at unit Reynolds numbers between 6.58×10^6 and 12.0×10^6/m. Distances are downstream of the nose tip. Reattachment is estimated to occur between 0.58 and 0.60 m. Legend applies to all figures.

peak exists between 50 and 170 kHz. This peak is not seen in the measurements made on the $3.5°$ flare without separation and is believed to be due to a shear-layer instability that is generated or amplified in the shear layer above the separation bubble. This instability also increases in amplitude with unit Reynolds number but does not change peak frequency. However, moving downstream,
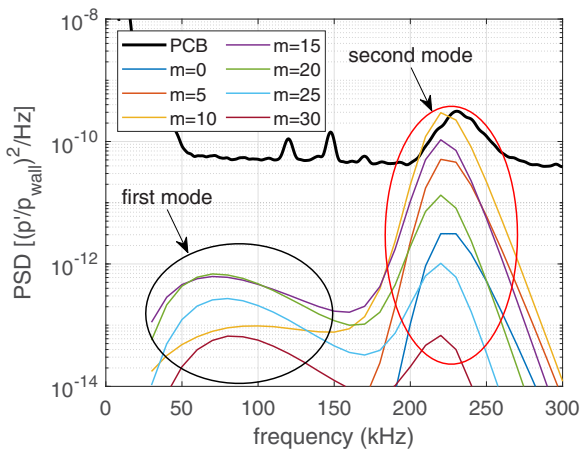
FIG. 21. Measured and computed surface pressure spectra on the cone, 0.387 m downstream of the nose tip. The vertical axis has been expanded to show the first mode from the computations. Re $= 11.5 \times 10^6$/m; data are from Paredes *et al.* [31].

the peak frequency tends to increase until the instability breaks down into two distinct peaks at the last PCB sensor. At this position, the shear-layer instability is present for only the highest three unit Reynolds numbers (in contrast to upstream stations, where lower unit Reynolds numbers also contain the instability). Global stability calculations have shown that the shear-layer instability is very near neutrally stable for this flare angle [31]; it is likely for this particular experiment that it is slightly on the stable side and begins to dampen out by the farthest downstream station.

Computations of this geometry reveal good agreement between the measured and computed surface pressure fluctuations. Figure 21 shows the measured and computed surface pressure fluctuations at one location on the cone. The computational results are displayed for several disturbance azimuthal wave numbers, *m*. The initial disturbance amplitude was selected such that the peak amplitude of the computed spectra matched that of this PCB measurement made near the end of the cone section at 0.387 m downstream of the nose tip. The first mode at this point is below the noise floor of the PCBs and therefore not measured. Figure 22 shows an example of the pressure fluctuations 0.606 m downstream of the nose tip, using the same initial amplitude set in the previous figure. The computed results were able to reproduce both the second-mode and shear-layer instabilities with accurate peak frequencies and bandwidths as compared to the surface pressure measurements. Oblique waves with $m = 10$ most closely reproduced the amplitudes measured by the PCB sensor. Comparable results were seen at the other PCB and Kulite sensor locations along the model. The PSE and HLNSE calculations show that the shear-layer instabilities are initiated as oblique first-mode waves over the cone. The results show that the first modes continue to amplify through the shear layer and lead to the low-frequency lobe in the spectra with comparable magnitude to the second-mode lobe. More computational results from this geometry can be found in Paredes *et al.* [31].

Based on the schlieren images described previously, reattachment near the maximum unit Reynolds number studied occurs between 0.58 and 0.60 m downstream of the nose tip. While the frequency peaks associated with the second-mode and shear-layer instabilities start to be seen just upstream of those locations [Fig. 20(a)], they are not coherent until reattachment. Figure 23 shows the power spectral densities and coherence for adjacent PCB sensors upstream and downstream of reattachment. Prior to reattachment, coherence levels are low. Sharp peaks seen between 100 and 200 kHz correspond to electronic noise that is also present in the PSDs. After reattachment, coherence values for both the shear-layer and second-mode instabilities are high, indicating that both are convective instabilities in the reattached boundary layer.
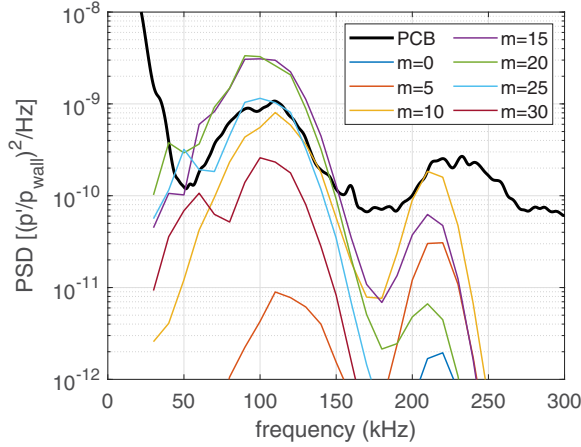
FIG. 22. Measured and computed surface pressure spectra along the cone 0.606 m downstream of the nose tip. The thick black line corresponds to the PCB measurement, and the colored lines correspond to the linear amplification of computed planar and oblique waves at different azimuthal wave numbers, *m*. Re = 11.5×10^6/m; data are from Paredes *et al.* [31].
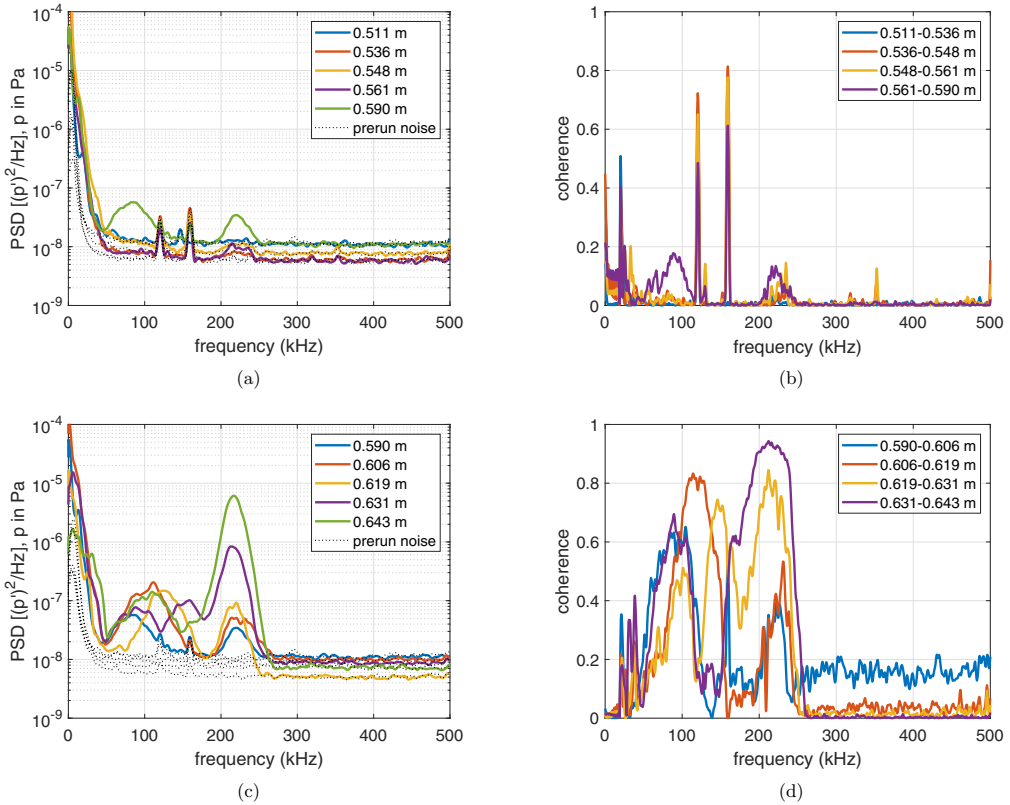

FIG. 23. Power spectral densities and coherences between PCB sensors upstream and downstream of reattachment along the 10° flare; Re = 11.4×10^6/m. High coherence values for all pairs downstream signify convective instabilities in the reattached boundary layer (a) PCB PSDs upstream of reattachment, (b) Coherence of PCB pairs upstream of reattachment, (c) PCB PSDs downstream of reattachment, and (d) Coherence of PCB pairs downstream of reattachment.
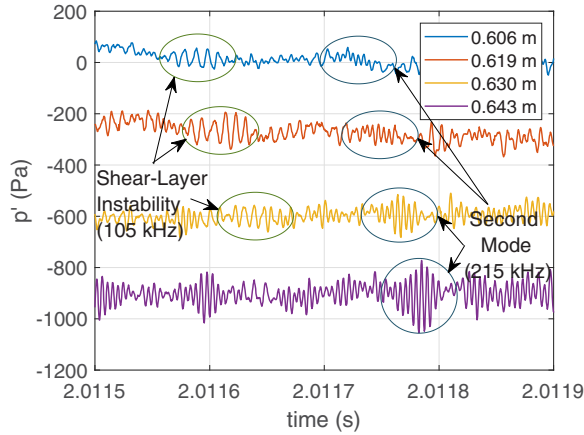
FIG. 24. Time series showing progression of shear-layer-instability traveling waves as well as the second mode in the reattached boundary layer. Re $= 12.0e6/m$.

Figure 24 includes sample time series from the four farthest downstream PCB sensors on the flare. These sensors are under the reattached boundary layer and are displayed offset from each other for clarity. In the time sample both shear-layer and second-mode wave packets appear. The shear-layer waves have a frequency of around 105 kHz, although they slightly increase in frequency moving downstream. The second mode has a frequency of about 215 kHz and remains relatively consistent in frequency. The distance between adjacent sensors is constant, so the slope of the line connecting each consecutive wave packet corresponds to the velocity of that packet; the shear-layer waves appear to traverse downstream at a faster velocity than the second-mode waves.

Due to their separation in frequency space, it is possible to bandpass filter the time series to isolate each instability. Therefore, the signals for downstream sensors can be cross-correlated to find their lag time, and from there find an estimate of the instability velocity. Figure 25 plots the lag times for the four farthest downstream PCB sensors, all located under the reattached boundary layer on the flare. The two bands, 50–170 kHz and 170–290 kHz, correspond to the frequency ranges of
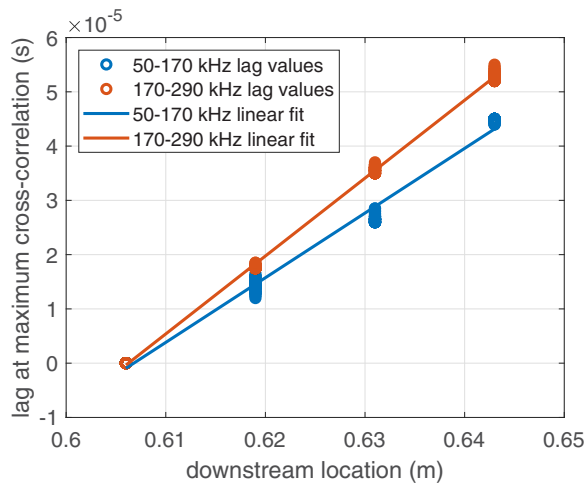

FIG. 25. Lag times used to estimate disturbance velocities for the shear-layer waves and second-mode waves. The data are accumulated from 60 runs across two entries. All results are at Re $= 11.6 \times 10^6/m$.
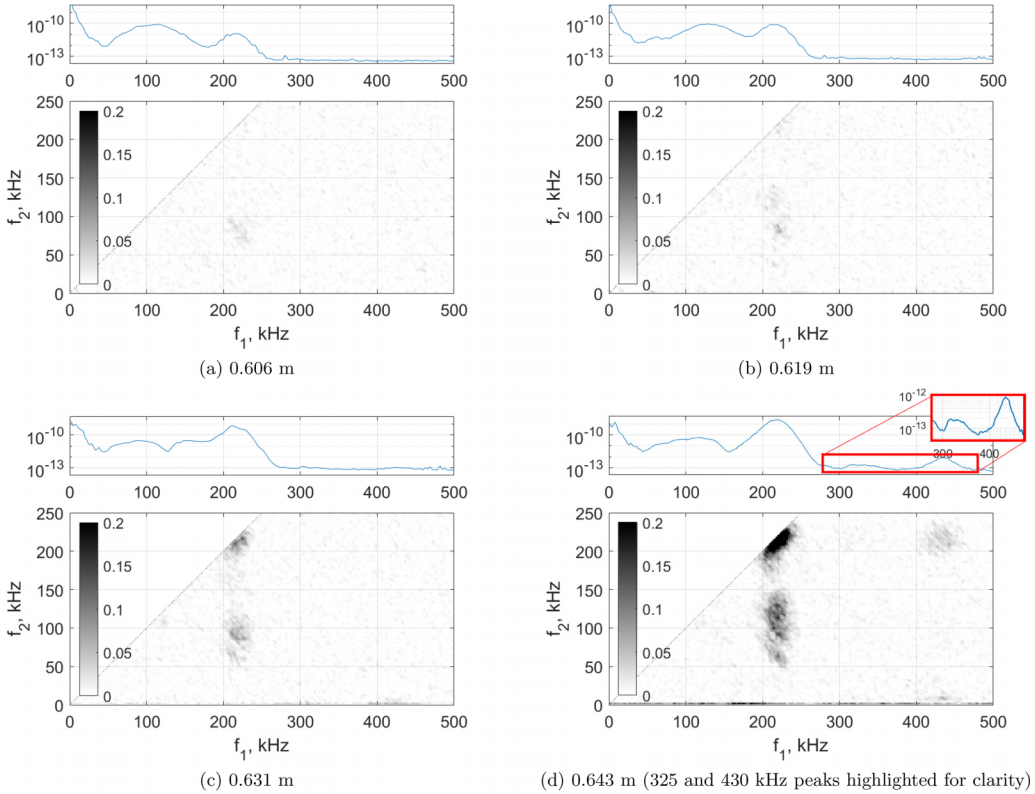
FIG. 26. Bicoherences for PCB sensors under reattached boundary layer on the flare. Upper plot displays power spectral density for the same data. Bicoherence significance threshold $b_{95}^2 = 0.0075$.

the shear-layer and second-mode instabilities, respectively. The plot includes 60 runs that all have a freestream unit Reynolds number of 11.6×10^6/m. By fitting the data from the two bands to a line, the shear-layer velocity was computed to be 843 m/s (about 102% of the computed shock-layer velocity), while the second mode was found to be 695 m/s (approximately 84% of the shock-layer velocity). The second-mode velocity is very similar to that on the $3.5°$ flare and therefore also near the slow acoustic wave velocity. It is possible, however, that the shear-layer waves may be aliased, which would mean their physical velocity of approximately half the shock-layer speed.

To determine whether nonlinear phase locking occurs between the two instabilities, as well as reveal the presence of harmonics, bicoherences of the PCB sensors under the reattached boundary layer on the flare were computed. The bicoherence was determined from Eq. (3), defined by Kim and Powers [61] and implemented in Matlab by Edelman [42]. In this equation, B is the bispectrum of a time series $x(t)$, and $X(f)$ is the Fourier transform of $x(t)$. The results of this analysis appear in Fig. 26, with the threshold for statistical significance ($b_{95\%}^2$) being 0.0075. This threshold is defined by $b_{95\%}^2 = 3/N$, where N is the number of averages used to compute the bicoherence and defines the value below which zero bicoherence can be assumed [42,62]. Values above this computed threshold therefore correspond to disturbances that are likely to have some level of nonlinear phase locking between them. Due to the large number of samples, only a relatively small bicoherence is necessary to demonstrate potential nonlinear phase locking. Initially, at 0.606 m downstream of the nose tip, only a small statistically significant bicoherence peak can be seen between the frequencies of 60–100 kHz and 200–250 kHz. This peak corresponds to a phase lock between the shear-layer and second-mode instabilities, which peak around 100 and 210 kHz, respectively.
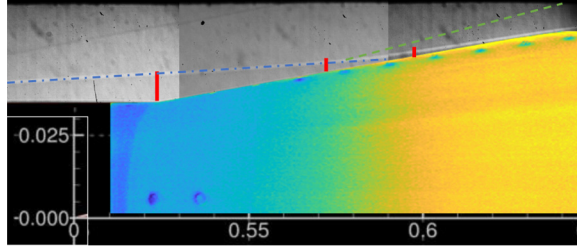
FIG. 27. FLDI sweep locations (red lines), with schlieren and heat flux overlays, Re = 11.5×10^6/m. Flow is from left to right. The shear layer is outlined with a blue dotted line, and the reattachment shock is extrapolated with a green dashed line. Note that, based on the schlieren measurements, reattachment is not believed to have occurred until around 0.58–0.60 m downstream. Therefore, the two upstream locations are likely both measurements of the shear layer, and the third is most likely the reattached boundary layer.

Downstream at 0.619 m, this bicoherence peak increases in amplitude. Additionally, another peak starts to emerge corresponding to second-mode harmonic generation for $f_1 = f_2 = 215$ kHz. These two peaks continue to amplify moving downstream at 0.631 m, and by 0.643 m a third peak appears for frequencies between 190–240 kHz and 400–460 kHz. This third peak is potentially a phase lock between the second mode and its harmonic:

$$b^2(f_1, f_2) = \frac{|B(f_1, f_2)|^2}{E\{|X(f_1)X(f_2)|^2\}E\{|X(f_1 + f_2)^2|\}}. \tag{3}$$

Both the shear-layer and second-mode instabilities are visible in the power spectral density plots above the bicoherences in Fig. 26. The shear-layer waves peak around 110 kHz, while the second mode is about 215 kHz. At the farthest downstream sensor, however, the PSD peaks corresponding to some of the bicoherence peaks begin to rise above the noise floor. The peak near 325 kHz is most likely from the phase lock between the two instabilities, as its frequency is the sum of the peaks corresponding to the shear-layer and second-mode waves. The peak near 430 kHz is the harmonic of the second mode, with its peak frequency equal to twice the second-mode peak frequency.

Given the excellent agreement between the linear computations and the experiment, and the fact that the flow remained laminar in the experiments, the nonlinear phase locking does not appear to have a major influence on the instability evolution. However, if a larger flare angle, higher freestream unit Reynolds number, or noisier flow were tested, it is possible that the initial phase locking observed here may impact the generation of turbulent spots. Prior experiments by Butler and Laurence have also demonstrated significant bicoherence levels indicating an interaction between the second-mode and the shear-layer instability under convention noise, transitional flow [23]. Additionally, later experiments conducted at the BAM6QT with a larger flare angle and slightly higher quiet unit Reynolds numbers provided similar results [63].

FLDI was used to make density gradient fluctuation measurements off the surface of the model. Measurements were made at a unit Reynolds number of 11.5×10^6/m. Three axial locations along the flare were selected for vertical sweeps that traversed from the surface through the shear or boundary layer. Figure 27 shows these locations over a composite schlieren image, with the shear layer highlighted by a blue dashed line and the reattachment shock extrapolated with a green dashed line. A heat flux image is also included to highlight the change in surface heat flux that occurs around reattachment, between 0.58 and 0.60 m downstream of the nose tip. Two of the FLDI positions are located upstream of reattachment, one right at the compression corner and one at 0.577 m. The third location is at 0.606 m downstream of the nose tip, just past reattachment in the boundary layer.

Figure 28 summarizes the density-gradient-fluctuation measurements made on this geometry. Each plot displays power spectral densities for different heights above the surface of the model,
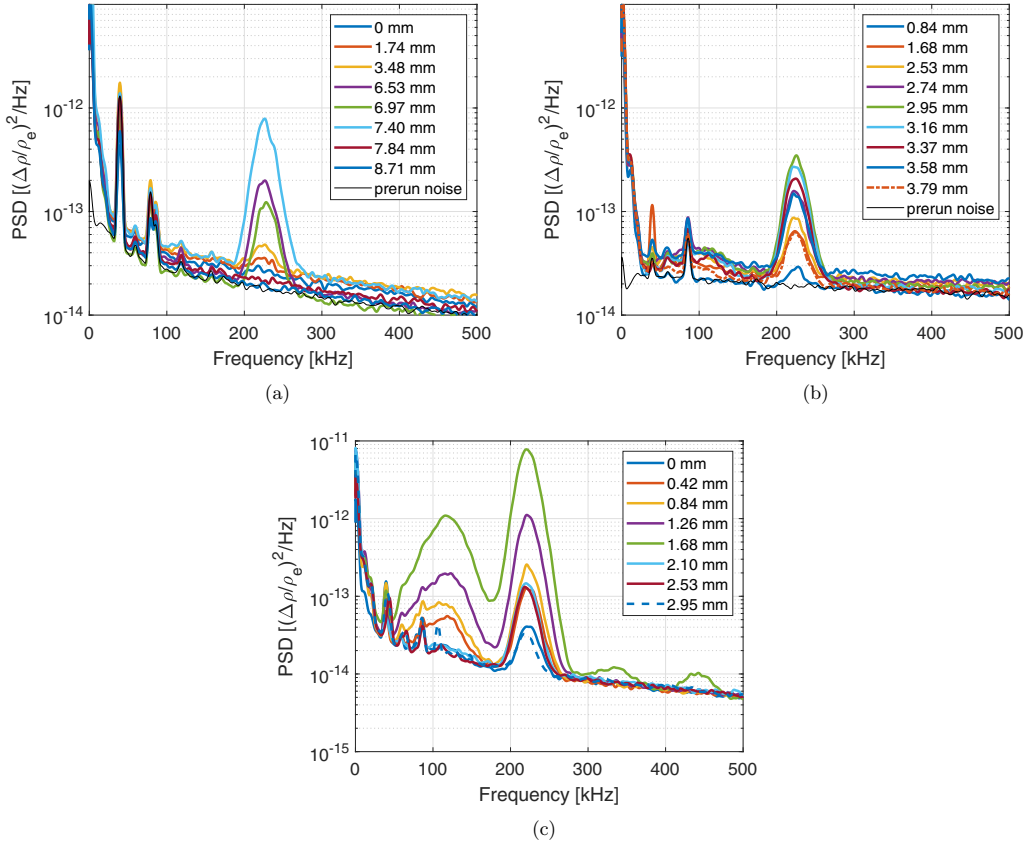
FIG. 28. FLDI density gradient fluctuation PSDs for Re = 11.5×10^6/m. Only second-mode waves can be seen in the shear layer at the compression corner. The shear-layer traveling waves start to rise up from the noise floor in measurements taken in the downstream portion of the shear layer. Distances in the legends correspond to heights off the surface. (a) 0.526 m downstream (at compression corner), (b) 0.577 m downstream (just upstream of reattachment), and (c) 0.606 m downstream (just downstream of reattachment).

normalized by the computed shear-layer or boundary-layer edge density at the given streamwise location. In Fig. 28(a) the FLDI measurements at the compression corner contain only one peak due to aerodynamic fluctuations, between 170 and 290 kHz. Peaks seen around 40 and 80 kHz are present in the prerun spectra and therefore correspond to electronic noise. The 170 to 290 kHz peak corresponds to the second mode and is at a maximum amplitude 7.40 mm off the surface. These data show that, while the second mode is not present in the surface pressure spectra under the bubble, it still exists in the shear layer above it. Farther downstream, in Fig. 28(b), the second mode can still be seen in the same frequency band. Additionally, rather than amplifying as it traverses downstream, the second-mode amplitude is lower at 0.577 m relative to at the compression corner (0.526 m). This suggests that the instability does not amplify as it traverses through the shear layer, a similar finding to computations and experiments on different geometries by Balakumar *et al.* [8] and Butler and Laurence [12]. In addition to the second mode, another peak can be seen centered around 100 kHz. This peak, which appears in the shear layer upstream of reattachment, represents the shear-layer instability that was measured in the surface pressure sensors under the reattached boundary layer.

FLDI measurements through the boundary layer just downstream of reattachment are shown in Fig. 28(c). Both the shear-layer and second-mode instabilities are present, with peaks around
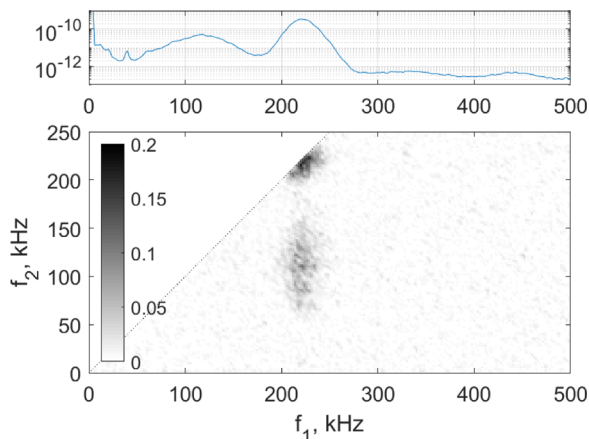
FIG. 29. Bicoherence for the FLDI in the reattached boundary layer above the flare, 0.606 m downstream of the nose tip. Bicoherence significance threshold $b_{95}^2 = 0.0075$.

110 and 210 kHz, respectively. Additionally, for both instabilities, the peak amplitude is measured 1.68 mm off the surface, which corresponds to the largest density gradient seen in the schlieren imagery at that location. At this off-surface point, two additional peaks can be seen around 320 and 420 kHz, which most likely represent a nonlinear interaction between the two instabilities, as well as a harmonic of the second mode. The amplitudes of the instabilities are also much greater at this axial position than they were along the shear layer upstream of reattachment.

The bicoherence for the FLDI measurements, as taken in the reattached boundary layer 0.606 m downstream of the nose tip, is shown in Fig. 29. Similar to the PCB bicoherences, it displays significant nonlinear phase locking between the shear-layer instability and the second mode, as well as the second-mode harmonic.

The computed density modes agree well with the off-surface FLDI measurements. Figure 30 plots the integrated FLDI measurements (integrated across 50 kHz) and the computed density modes (scaled to match the farthest upstream FLDI measurement at 210 kHz). Note that, based on the computations, the density peaks appear to be produced by the planar modes ($m = 0$), while the pressure peaks were produced by oblique modes (as seen in Fig. 22). In general, the shape of the computed fluctuations resemble those from the experiment, although the amplitudes vary more between the shear-layer (110 kHz) and second-mode (210 kHz) instabilities with the FLDI than in the computations. In particular, the predicted point of peak fluctuation was found to be within 12.5% of the measured peak location for each case.

C. Artificial disturbance propagation

A plasma perturber was integrated into the model to further study this shear-layer instability and see what a breakdown to turbulence under quiet flow might look like for this geometry. This perturber was used to generate large-amplitude controlled disturbances into the boundary layer, which would create wave packets that could be tracked as they convected downstream. The electrodes were placed at the downstream end of the cone section [see Fig. 4(b)], providing the large initial disturbance downstream of the region of second-mode amplification but upstream of the separation bubble. By placing them at this point, any instability amplified by the shear layer over the bubble should result in higher-amplitude waves at reattachment when the perturber is on than when it is off. However, if an instability is not amplified by the shear layer, its amplitude should not be affected by the artificial disturbances.
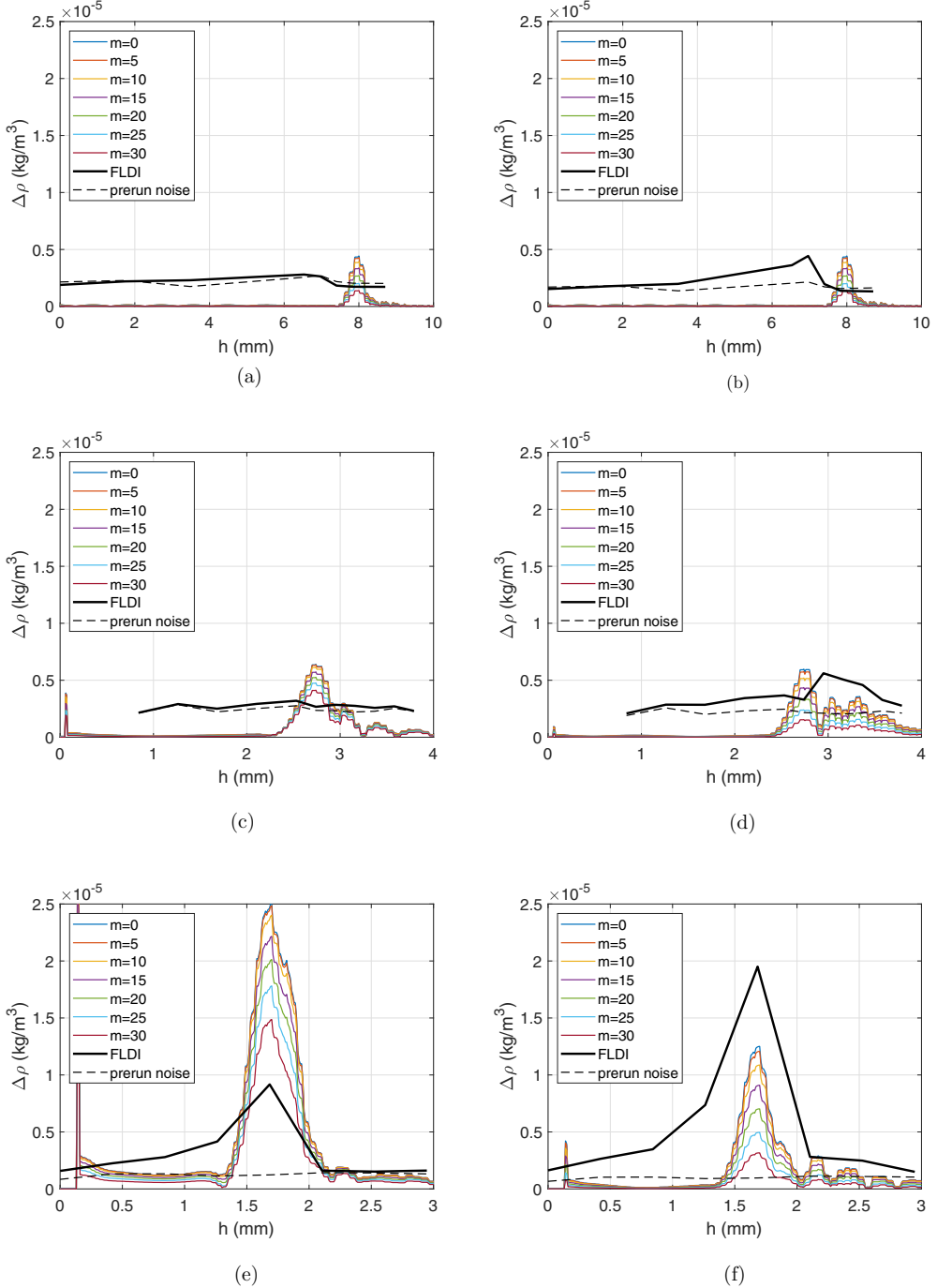
FIG. 30. Integrated FLDI amplitudes (integrated across 50 kHz centered at the labeled frequency) as compared to computed density modes. Re $= 11.5 \times 10^{6}$/m. (a) 0.526 m downstream (at compression corner), 110 kHz, (b) 0.526 m downstream (at compression corner), 210 kHz, (c) 0.577 m downstream (just upstream of reattachment), 110 kHz, (d) 0.577 m downstream (just upstream of reattachment), 210 kHz, (e) 0.606 m downstream (just downstream of reattachment), 110 kHz, and (f) 0.606 m downstream (just downstream of reattachment), 210 kHz.

TABLE I. Run conditions and pulser settings for plasma perturber study.

Run	Re (m^{-1})	P_0 (pounds per square inch absolute)	T_0 (K)	T_w (K)	Pulse duration (ns)	Frequency (kHz)	Number of pulses	Voltage (kV)
1232	11.6×10^6	148.01	417.03	321	100	2	300	7.5
1211	11.6×10^6	147.96	416.17	321	100	2	300	10.0
1228	11.6×10^6	148.76	418.79	321	100	2	300	12.5
1231	10.3×10^6	131.57	416.62	321	100	2	300	12.5
1230	8.91×10^6	112.95	415.42	321	100	2	300	12.5
1229	7.39×10^6	94.20	416.94	321	100	2	300	12.5

Six runs with varying conditions were selected to demonstrate the results of the plasma perturbation experiment. The run conditions are summarized in Table I. Two key variables were altered between these runs: perturber voltage and freestream unit Reynolds number. The input voltage was varied between 7.5 and 12.5 kV, and then held at 12.5 kV for the unit Reynolds number runs. The unit Reynolds numbers selected range from a case where no natural instabilities are measurable under quiet flow to the maximum quiet value available at the time.

The disturbances generated by the perturber were short-duration pulses at 2 kHz that were designed to have a relatively flat frequency response for a frequency band of the natural instabilities of the flow. Figure 31 displays individual pulses' current and voltage values as well as their associated FFTs. Two pulses are shown: one at atmospheric pressure with no flow but with high resolution and one captured during a run with Re $= 11.6 \times 10^6$/m but with lower resolution. Both pulses have very similar shapes for current, but the pulse was wider in voltage during the run. Nevertheless, both the atmospheric and Re $= 11.6 \times 10^6$/m cases have flat frequency responses to nearly 5 MHz, well above the 300 kHz band that contains the instabilities of interest.

The perturber would generate a sharp, high-amplitude electronic noise spike every time it actuated. This noise spike raised the noise floor of the power spectral density analysis of the runs, potentially obscuring instability frequency peaks. Previous work by McKiernan used a Hampel filter to help remove this spike and consequentially lower the noise floor [17,18]. However, since the frequency of the perturber is known and allows for sufficient time between the pulse generation and the measurement of the resulting wave packet, it is possible to manually remove the spike completely without affecting the instability measurements. Using the established perturber timing, the data for 7×10^{-5} seconds at the time of each electrical spike are replaced with the mean pressure value from the five data points immediately prior to the spike. Figure 32 plots an example showing the noise spike and resulting wave packet, as well as a power spectral density plot for three different instances of the same data. The first instance corresponds to the raw data without any filtering, while the second shows the Hampel filter. Finally, the manual noise removal method is shown. While the Hampel filter does significantly reduce the noise floor, it never reaches the prerun electronic noise level by 500 kHz. However, the manual noise removal method reaches the prerun level by 400 kHz, without any negative effects on the instability peak measured at 100 kHz. This is the method used to analyze the perturber results.

Power spectral densities for PCB sensors on the flare surface at and downstream of reattachment for the different perturber voltages are displayed in Fig. 33. All runs were at Re $= 11.6 \times 10^6$/m. A higher perturber voltage corresponds to a larger initial disturbance amplitude at the electrodes, which then can be amplified as it traverses downstream through the shear layer. In general, the higher the voltage, the larger the measured pressure fluctuation amplitudes along the flare. Additionally, with higher voltages, the power spectra begin to broaden farther upstream. For example, the 12.5 kV case has broadband energy that includes the 300–400 kHz band at 0.619 m downstream of the nose tip, while the 7.5 kV case does not have significant broadband energy until 0.643 m. The unperturbed case never broadens by the end of the model. This broadening

(a) Individual current pulses.

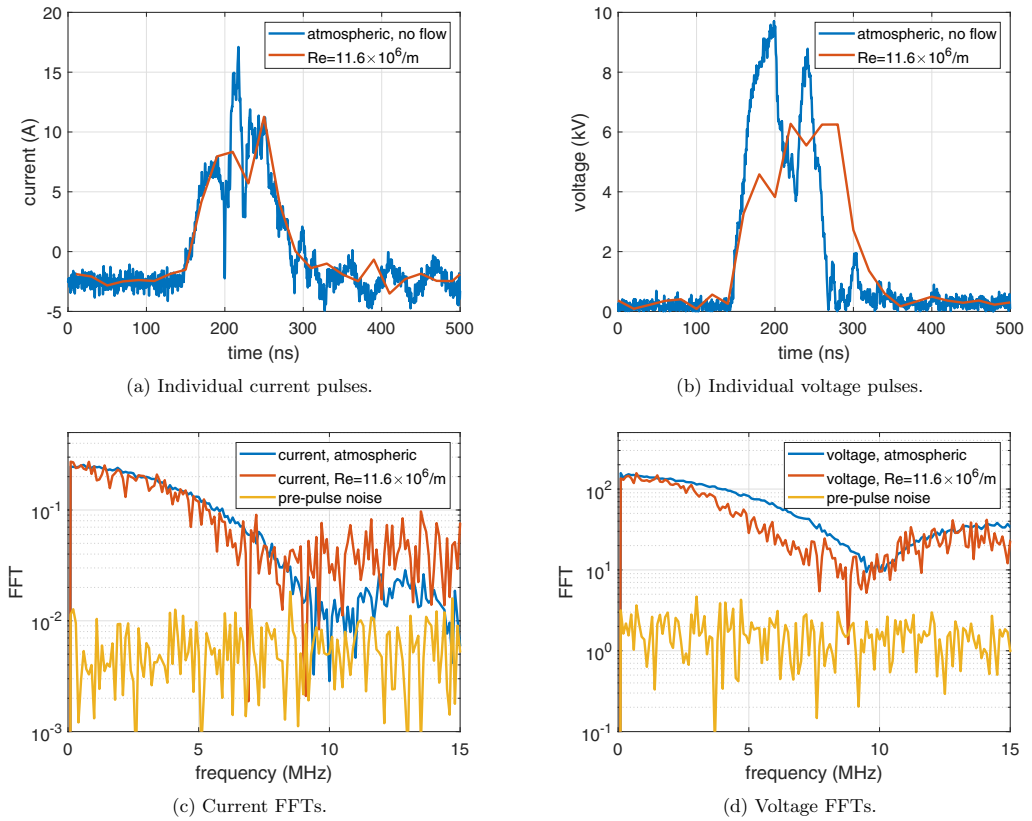(b) Individual voltage pulses.

(c) Current FFTs.

(d) Voltage FFTs.

FIG. 31. Plasma perturber pulse samples and FFTs. Pulses were generated at atmospheric pressure without flow to see a high-resolution image of the shape, while lower-resolution data were captured during each run.

of the spectra can potentially indicate the generation of turbulent spots and onset of transition, or can indicate enhanced nonlinear interactions. In either case this broadening is seen only with the
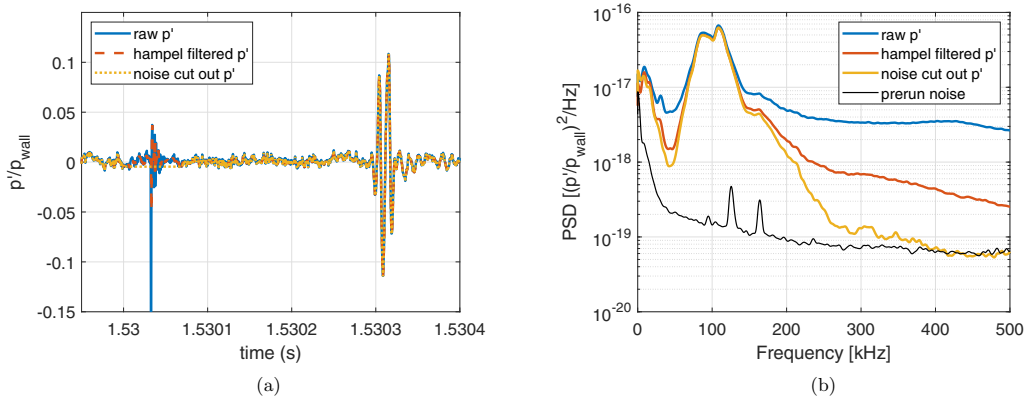

FIG. 32. Noise-filtering methods used with the perturber data. (a) Pressure time series highlighting different filtering methods and (b) Pressure PSDs for each filtering method.
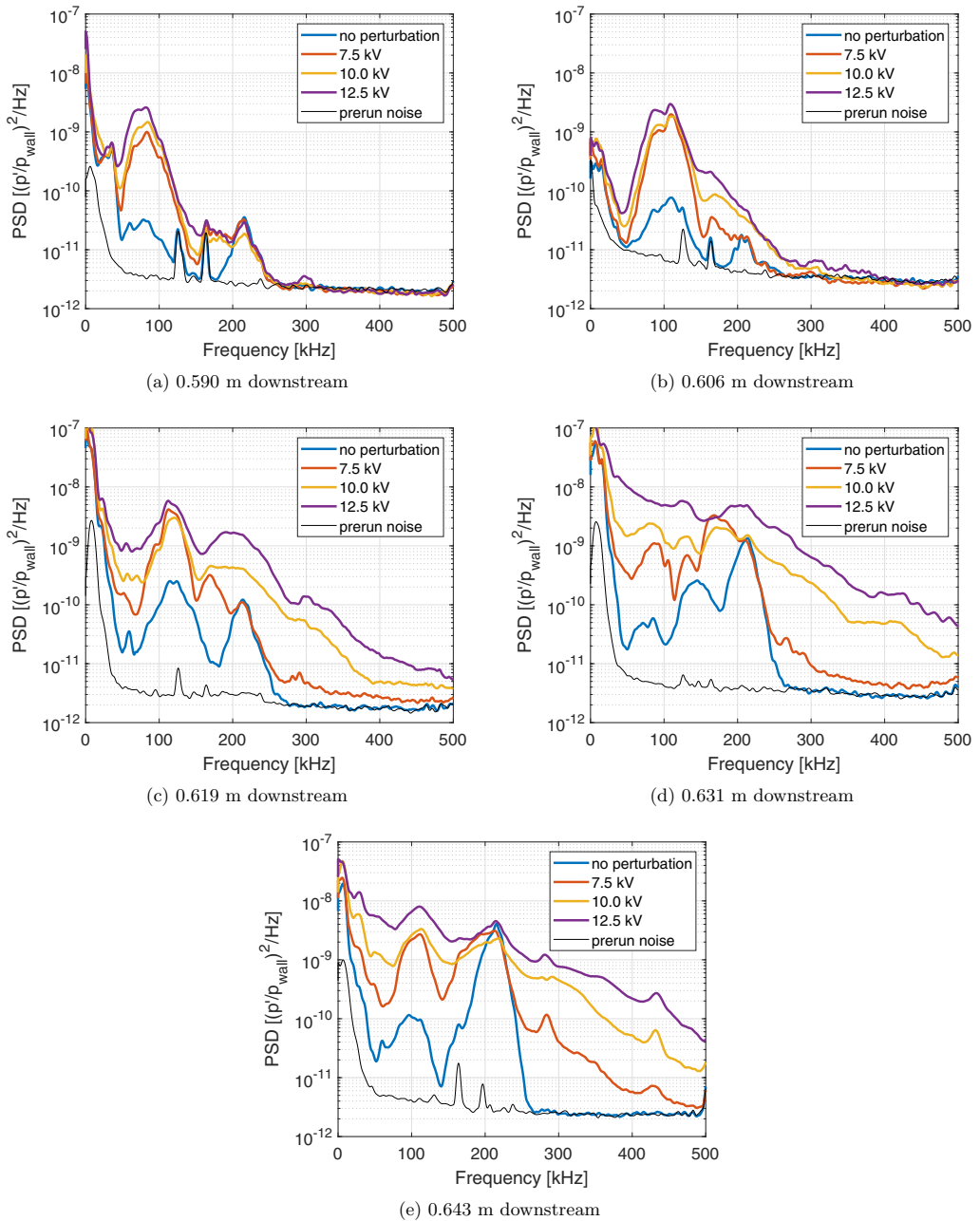
(a) 0.590 m downstream

(b) 0.606 m downstream

(c) 0.619 m downstream

(d) 0.631 m downstream

(e) 0.643 m downstream

FIG. 33. Power spectral densities for PCBs in the reattached boundary layer with different pulser voltages. Re $= 11.6 \times 10^6$/m.

larger initial amplitudes provided by the perturber under quiet flow and not during the unperturbed measurements.

In addition to highlighting the voltage trends, Fig. 33(a) likely supports the conclusion that the shear-layer instability, but not the second mode, is amplified by the presence of the separation bubble. The PCB sensor for this location is at the reattachment point along the flare, and its spectra

contain two distinct peaks. The peak at around 90 kHz corresponds to the shear-layer instability, while the one at around 210 kHz is from the second mode. The peak frequencies for the two instabilities remain the same with and without perturbation; however, the peak amplitudes for the shear-layer instability are much greater with perturbation, while the second-mode amplitudes are unchanged at reattachment. The perturber electrodes are located downstream of the cone but upstream of the separation bubble and provide a flat response to 5 MHz. However, since the electrodes are upstream of the expansion, there are to two possible conclusions from the downstream sensor PSD:

(1) The initially flat response, after being processed through the expansion, is damped more for higher frequencies (such as those for the second mode) than lower ones (such as those for the shear-layer instability). This processed response is then amplified as it convects through the shear layer, resulting in the PSD as shown in Fig. 33(a). In this case nothing can be determined about the relative amplification rates of the second-mode and shear-layer instabilities in the region of the bubble.

(2) The initially flat response is damped relatively equally across the frequencies of interest as it is processed through the expansion. This still-flat processed response is then amplified as it convects through the shear layer, with the shear-layer-instability frequencies amplified more than the second-mode frequencies.

While PCB and Kulite data were collected along the cylinder, the electrical interference of the perturber was too intense to successfully mitigate, so it is not possible to definitively state which case is present in the flow. However, previous evidence has been obtained on a cone-cylinder model at Mach 6 that shows signals as low as 55 kHz being damped by the expansion [11]. Additionally, both experimental and computational studies have previously shown that the second mode is neutrally stable in a hypersonic shear layer [8,12,23]. Therefore, it is likely that case 2 is the dominant physical explanation. The shear-layer instability is amplified in the shear layer, while the second-mode instability resumes amplification downstream of reattachment.

The 12.5 kV setting was selected for the freestream unit Reynolds number sweep. The power spectral densities for those results, as compared with the natural unperturbed spectra, are plotted in Fig. 34. For the natural cases, the shear-layer fluctuations (between 50 and 170 kHz) and the second mode (between 170 and 290 kHz) can be seen in all sensors for the two highest unit Reynolds numbers. Low-amplitude fluctuations are visible for the $Re = 8.91 \times 10^6$/m case for the downstream sensors, while no natural fluctuations are evident for the $Re = 7.39 \times 10^6$/m case. With all four unit Reynolds numbers, there is no peak broadening through the farthest downstream sensor. For the 12.5 kV perturbed cases, fluctuations in the frequency band of the shear-layer instability exist for all unit Reynolds numbers, with higher values corresponding to greater amplitudes. Additionally, moving downstream under the highest unit Reynolds numbers, the instability peaks begin to broaden, potentially indicating the onset of boundary-layer transition or at least enhanced nonlinear interactions. This broadening occurs farther upstream for the $Re = 11.58 \times 10^6$/m case than the $Re = 10.33 \times 10^6$/m one.

A continuous wavelet transform (CWT) analysis was performed for the highest-Re case to get a better understanding of which instability (the shear-layer or second-mode) is leading to the higher-frequency energy. Four wave packets from each sensor are shown in Fig. 35 for the reattached boundary layer. Time series of the same data are displayed in Fig. 36. The wave packets clearly first develop in the 50–100 kHz band that the shear-layer instability resides. As the packets convect downstream, they broaden in frequency to eventually spread out to over 400 kHz by the 0.643 m downstream of the nose tip. At this farthest downstream station, second-mode wave packets begin to appear outside of the region seeded by the perturber (note that the gaps in the second-mode band preceding each wave packet correspond with the parts of the time series that were cut and replaced with the mean). The time series data show the four wave packets amplifying as they convect in the boundary layer. An enhanced view showing just the first wave packet reveals a very sinusoidal structure for the first two packets, which gradually becomes irregular and distorted by the last station.
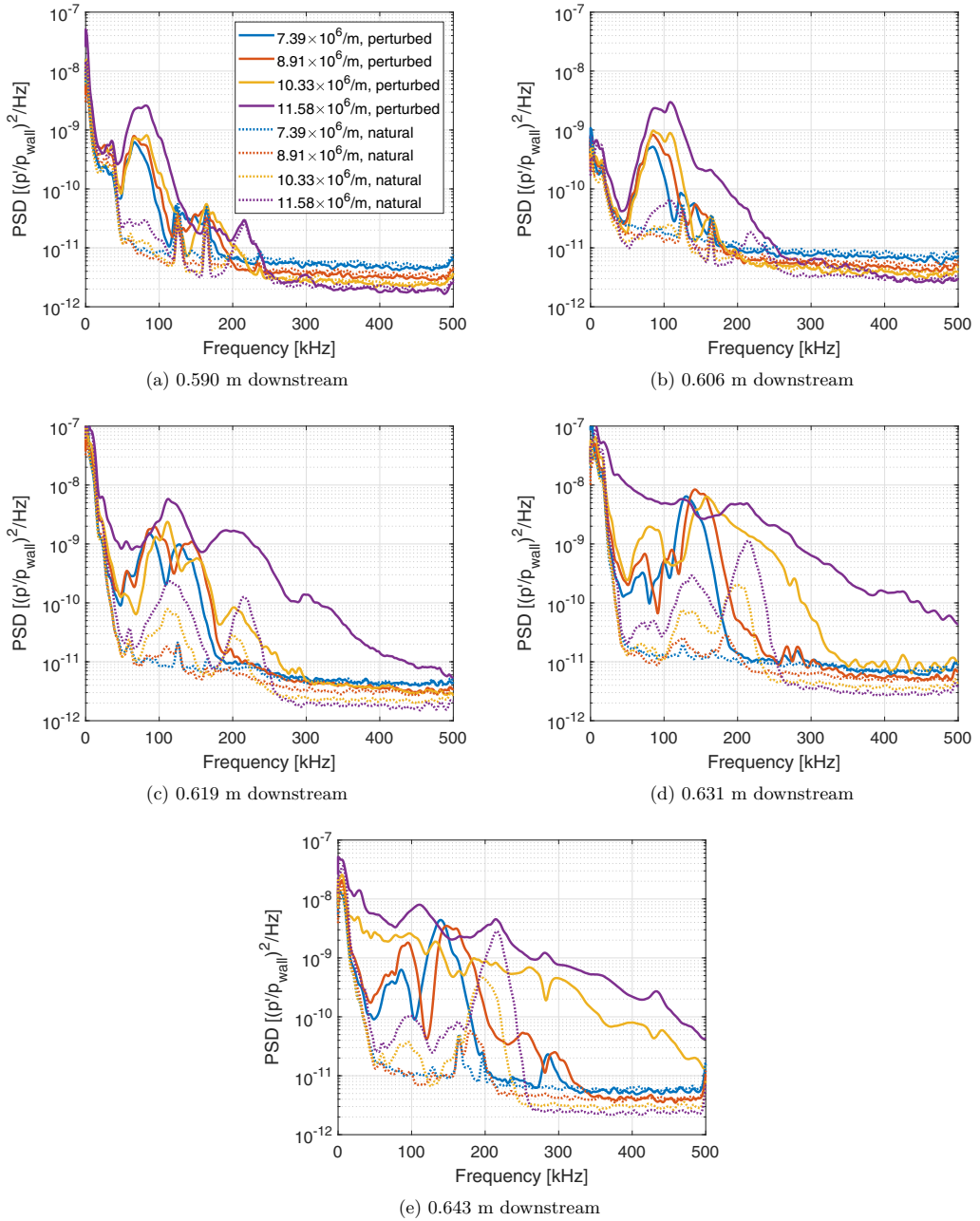
FIG. 34. Power spectral densities for PCBs in the reattached boundary layer at different unit Reynolds numbers with and without 12.5 kV controlled disturbances. Legend applies to all figures.

The surface pressure fluctuation RMS amplitudes, integrated between 50 and 270 kHz, for both the perturbed and unperturbed cases are shown in Fig. 37. The amplitudes are plotted as a function of the local Reynolds number with the reference length equal to each sensor's axial position relative to the compression corner. For the natural, unperturbed cases, amplification of the surface pressure fluctuations is not measured until around $\mathrm{Re}_x = 10 \times 10^5$. However, amplification of the perturbed

(a) 0.590 m downstream

(b) 0.606 m downstream

(c) 0.619 m downstream
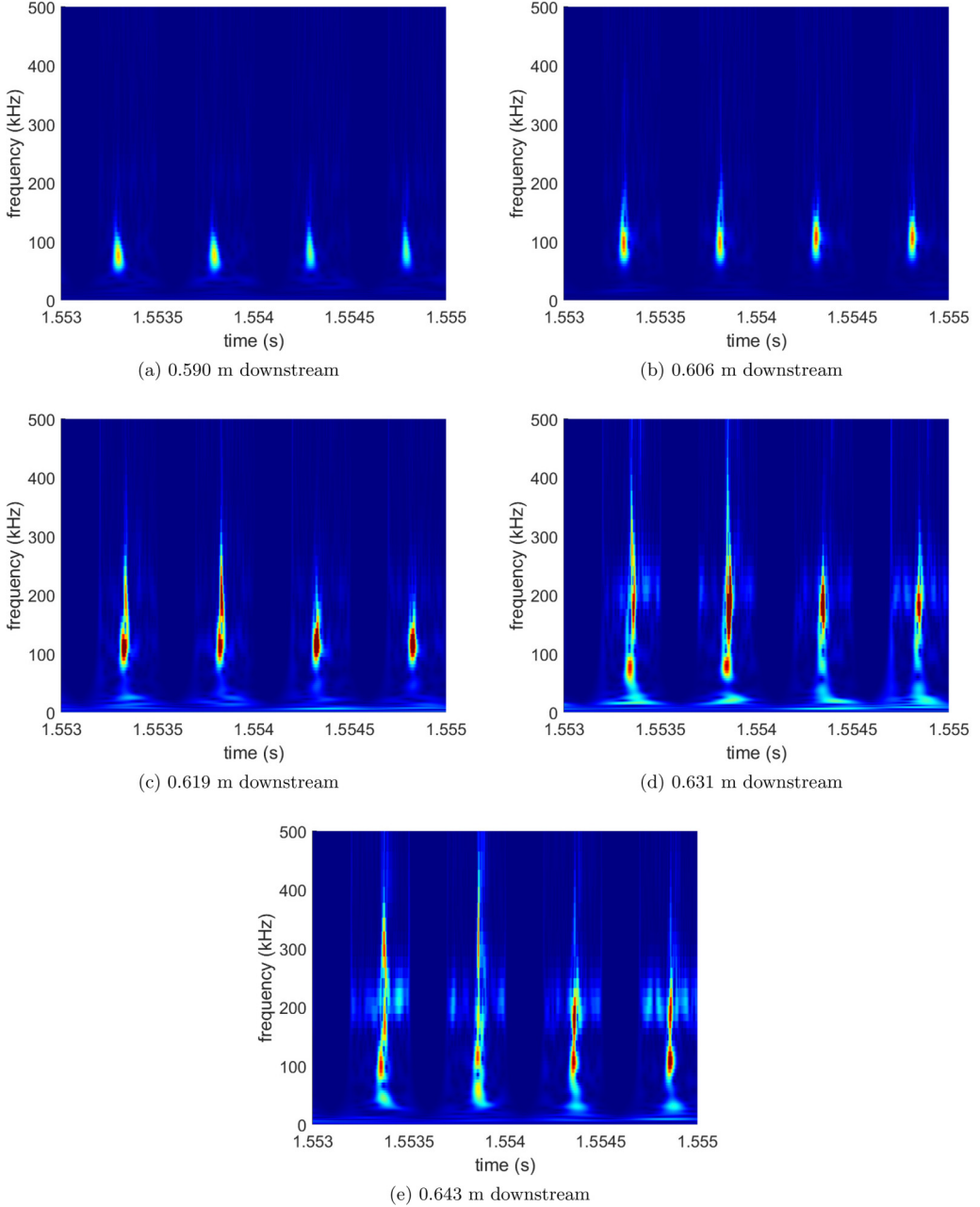
(d) 0.631 m downstream

(e) 0.643 m downstream

FIG. 35. CWT plots for PCBs in the reattached boundary layer with 12.5 kV controlled disturbances. Color scale is the same for all images. $Re = 11.6 \times 10^6$/m.

cases was detected at least as low as $Re_x = 2 \times 10^5$. Perturbed amplitudes were consistently higher than unperturbed amplitudes. This differs from results found by McKiernan on an Oberkampf geometry [17,18]. In his case, the perturbed and unperturbed cases coincided as the same length Reynolds numbers, and there was no change in transition Reynolds number between the two cases.
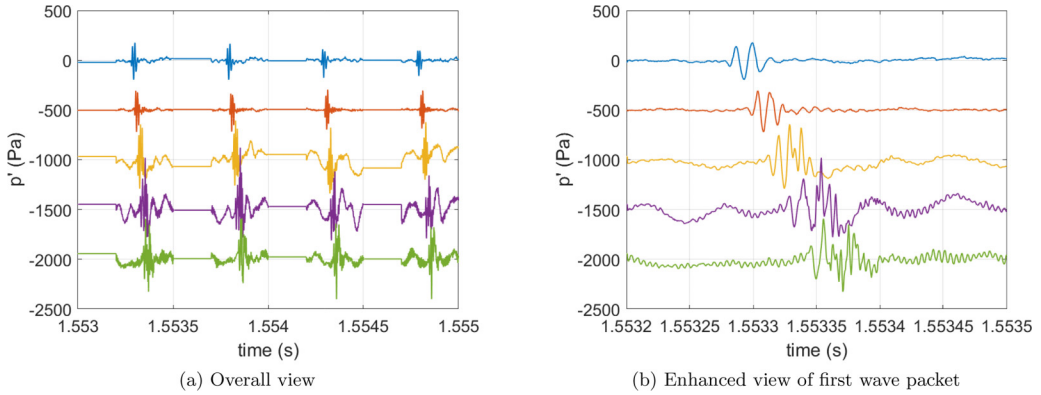
(a) Overall view

(b) Enhanced view of first wave packet

FIG. 36. Time series for PCBs in the reattached boundary layer with 12.5 kV controlled disturbances. $Re = 11.6 \times 10^6$/m.

FLDI measurements were made in the shear layer 3 mm off the surface of the model and 0.577 m downstream of the nose tip. Figure 38 plots the power spectral densities for the four unit Reynolds numbers tested for the perturbed and unperturbed cases. For the natural results, only the second-mode fluctuations are visible, and only for the two highest unit Reynolds numbers. This most likely differs from previous natural FLDI results due to a combination of a higher noise floor present in the FLDI measurements during the perturber entry and suboptimal off-surface placement of the beams [variation in FLDI peak amplitude can be seen as a function of off-surface height in Fig. 28(b)]. When the perturber is on, higher energy levels are measured for all unit Reynolds numbers in the 50 to 170 kHz band associated with the shear-layer instability, while the second-mode peak amplitudes remain constant. This result, like the outcome for the PCB at reattachment, highlights the fact that the 50 to 170 kHz instability is related to amplification in the shear layer, while the second mode traverses through the shear layer without any amplification.

V. CONCLUSION

A series of experiments were conducted to study hypersonic instabilities present on a cone-cylinder-flare geometry at Mach 6. A sharp, $5°$ half-angle cone, followed by a cylinder with either
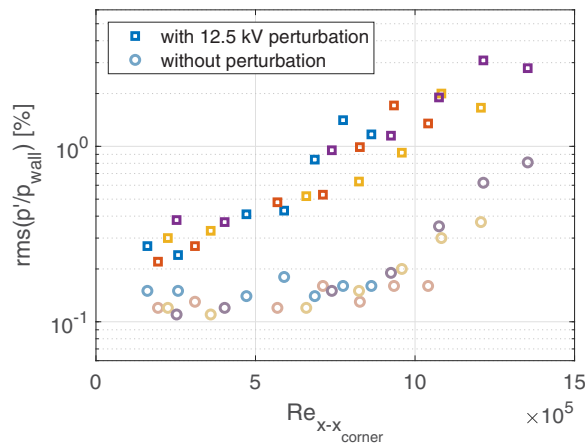

FIG. 37. Integrated RMS amplitudes with and without perturbation (integrated between 50 and 270 kHz).
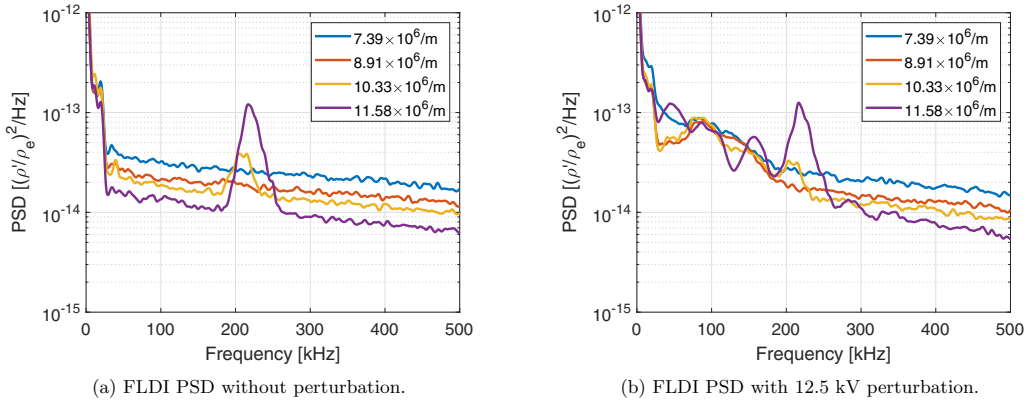
(a) FLDI PSD without perturbation.

(b) FLDI PSD with 12.5 kV perturbation.

FIG. 38. FLDI PSDs with and without perturbation. FLDI beams were located 3 mm off the surface and 0.577 m downstream of the nose tip.

a $3.5°$ or $10°$ flare was tested under quiet flow at the Boeing/AFOSR Mach-6 Quiet Tunnel (BAM6QT). The $3.5°$ flare was designed to compress but not separate the flow, while the $10°$ flare was designed to induce an axisymmetric separation bubble through shock–boundary-layer interactions (SBLIs). For both models under quiet flow, the flow remained laminar at all unit Reynolds numbers tested.

With the $3.5°$ flare, heat flux and surface pressure fluctuation measurements were taken at a near-zero angle of attack. The normalized heat flux was relatively constant along the flare. The second-mode instability was present in surface pressure measurements along the cone, peaking between 200 and 300 kHz depending on the unit Reynolds number. This instability was damped out as it passed through the expansion to the cylinder and returned along the flare. No other aerodynamic instabilities were identified along the flare, and the second mode amplified through the downstream end of the model.

With the $10°$ flare, heat flux, surface pressure fluctuation, and off-the-surface density-gradient fluctuation measurements, as well as schlieren images, were taken at near-zero angle of attack. The separation bubble at the compression corner remained physically stationary under quiet flow, but shear-layer movement was clearly visible under conventional noise. Reattachment was estimated to occur between 0.579 and 0.600 m downstream of the nose tip for the highest-Re case. Heat-transfer measurements showed an increase in heat along the flare up until just after the estimated reattachment location, where the heat flux began to plateau. As with the $3.5°$ flare version, the second mode was present along the cone and dampened out over the cylinder. Pressure and density fluctuation measurements along the shear layer and reattached boundary layer revealed both the second-mode between 170 and 290 kHz, and another instability between 50 and 170 kHz. This lower-frequency instability is believed to be a shear-layer instability, as it was not present in the boundary layer of the smaller-angle flare, which does not have a separation bubble. Computations revealed that this instability is oblique and is amplified along the shear layer. Bicoherence plots also showed that nonlinear phase locking occurred between the second-mode and the shear-layer instabilities.

Artificial disturbances generated by a plasma perturber were input into the boundary layer of the $10°$ flare model at the downstream end of the cone. This placed the generated disturbances downstream of the primary second-mode amplification region but upstream of the separation bubble. The shear-layer instability, but not the second mode, had a higher pressure fluctuation amplitude with perturbation than without. FLDI measurements picked up the shear-layer instability in the shear layer when the perturber was active but only the second-mode when it was not. The second-mode amplitudes from the FLDI were also unchanged when using controlled disturbances.

The perturber experiments provide additional evidence that the second mode is neutrally stable in the shear layer. The shear-layer instability, however, amplifies as it convects through the shear layer. These experiments also show a potential breakdown initiated with the shear-layer instability. Therefore, this instability might be a potential mechanism for transition to turbulence under the right conditions.

Overall, with the $3.5°$ flare, only the second mode is seen, while with the $10°$ flare an additional shear-layer instability is present. The dominant instability will depend on the flow conditions. With the sharp-nose, axisymmetric geometry at a near-zero angle of attack as studied in this case, the shear-layer instability appears neutrally stable downstream of reattachment for a $10°$ flare. For a hypersonic vehicle in flight, with varying conditions such as angle of attack, Mach number, and wall temperature, the dominant instability remains to be determined.

ACKNOWLEDGMENTS

[1] H. Babinsky and J. Harvey, *Shock Wave-Boundary-Layer Interactions* (Cambridge University Press, 2014).

[2] K. Stewartson and P. Williams, Self-induced separation, Proc. R. Soc. London A **312**, 181 (1969).

[3] J. Becker and P. Korycinski, Heat transfer and pressure distribution at a Mach number of 6.8 on bodies with conical flares and extensive flow separation, Tech. Rep. RM L56F22, NACA, Langley Field, VA, 1956.

[4] D. Chapman, D. Kuehn, and H. Larson, *Investigation of separated flows in supersonic and subsonic streams with emphasis on the effect of transition*, Tech. Rep. No. 1356, NACA, Moffett Field, CA, 1958.

[5] D. Dolling, Wall pressure fluctuations in a supersonic separated compression ramp flowfield, in *3rd Joint Thermophysics, Fluids, Plasma and Heat Transfer Conference, St. Louis, MO* (AIAA, 1982).

[6] L. Vandomme, B. Chanetz, R. Benay, and J. Parraud, Shock wave transitional boundary layer interaction in hypersonic flow, in *12th AIAA International Space Planes and Hypersonic Systems and Technologies, Norfolk, VA* (AIAA, 2003).

[7] R. Benay, B. Chanetz, B. Mangin, L. Vandomme, and J. Perraud, Shock wave/transitional boundary-layer interactions in hypersonic flow, AIAA J. **44**, 1243 (2006).

[8] P. Balakumar, H. Zhao, and H. Atkins, Stability of hypersonic boundary layers over a compression corner, AIAA J. **43**, 760 (2005).

[9] E. Benitez, J. Jewell, S. Schneider, and S. Esquieu, Instability measurements on an axisymmetric separation bubble at Mach 6, in *AIAA Aviation 2020 Forum, Virtual Event* (AIAA, 2020).

[10] E. Benitez, J. Jewell, and S. Schneider, Propagation of controlled disturbances through an axisymmetric separation bubble at Mach 6, in *AIAA Aviation 2021 Forum, Virtual Event* (AIAA, 2021).

[11] C. Butler and S. Laurence, Interaction of hypersonic boundary-layer instability waves with axisymmetric compression and expansion corners, in *AIAA Aviation 2020 Forum, Virtual Event* (AIAA, 2020).

[12] C. Butler and S. Laurence, Interaction of second-mode disturbances with an incipiently separated compression-corner flow, J. Fluid Mech. **913**, R4 (2021).

[13] A. Dovgal, V. Kozlov, and A. Michalke, Laminar moundary layer separation: Instability and associated phenomena, Prog. Aerospace Sci. **30**, 61 (1994).

[14] N. Sandham and W. Reynolds, Compressible mixing layer: Linear theory and direct simulation, AIAA J. **28**, 618 (1990).

[15] J. Edelman, B. Chynoweth, G. McKiernan, C. Sweeney, and S. Schneider, Instability measurements in the Boeing/AFOSR Mach-6 quiet tunnel, in *46th AIAA Fluid Dynamics Conference, Washington, DC* (AIAA, 2016).

[16] B. Chynoweth, J. Edelman, K. Gray, G. McKiernan, and S. Schneider, Measurements in the Boeing/AFOSR Mach-6 quiet tunnel on hypersonic boundary-layer transition, in *47th AIAA Fluid Dynamics Conference, Denver, CO* (AIAA, 2017).

[17] G. McKiernan, Instability of the shear layer on a sliced cone with finite span compression ramps at Mach 6, Ph.D. thesis, Purdue University, West Lafayette, IN, 2020.

[18] G. McKiernan and S. Schneider, Instability and transition on a cone with a slice and ramp at Mach 6, in *AIAA Scitech 2021 Forum, Virtual Event* (AIAA, 2021).

[19] W. Oberkampf and D. Aeschliman, Joint computational/experimental aerodynamics research on a hypersonic vehicle, part I: experimental results, AIAA J. **30**, 2000 (1992).

[20] M. Leinemann, R. Radespiel, F. Muñoz, S. Esquieu, G. McKiernan, and S. Schneider, Boundary layer transition on a generic model of control flaps in hypersonic flow, in *AIAA Scitech 2019 Forum, San Diego, CA* (AIAA, 2019).

[21] A. Pandey, K. Casper, R. Spillers, M. Soehnel, and S. Spitzer, Hypersonic shock wave–boundary-layer interaction on the control surface of a slender cone, in *AIAA Scitech 2020 Forum, Orlando, FL* (AIAA, 2020).

[22] A. Pandey, K. Casper, D. Guildenbecher, S. Beresh, R. Bhakta, M. De Zetter, and R. Spillers, Instability measurements in hypersonic flow on a three-dimensional cone-slice-ramp geometry, in *AIAA Scitech 2022 Forum, San Diego, CA & Virtual* (AIAA, 2022).

[23] C. Butler and S. Laurence, Transitional hypersonic flow over slender cone/flare geometries, J. Fluid Mech. **949**, A37 (2022).

[24] M. Lugrin, S. Beneddine, C. Leclercq, E. Garnier, and R. Bur, Transition scenario in hypersonic axisymmetrical compression ramp flow, J. Fluid Mech. **907**, A6 (2021).

[25] J. Ginoux, Investigation of flow separation over ramps at $M_\infty = 3$, Tech. Rep. No. AEDC-TR-65-273, Von Kármán Gas Dynamics Facility, Arnold Engineering Development Center, Arnold Air Force Station, TN, 1965.

[26] G. Inger, Three-dimensional disturbances in high speed boundary layer flows, Tech. Rep. No. 82-0110, AFOSR, Bolling Air Force Base, DC, 1981.

[27] M. Lugrin, S. Beneddine, E. Garnier, and R. Bur, Multi-scale study of the transitional shock-wave boundary layer interaction in hypersonic flow, Theor. Comput. Fluid Dyn. **36**, 277 (2022).

[28] S. Cao, J. Hao, I. Klioutchnikov, H. Olivier, and C. Wen, Unsteady effects in a hypersonic compression ramp flow with laminar separation, J. Fluid Mech. **912**, A3 (2021).

[29] S. Cao, J. Hao, I. Klioutchnikov, C. Wen, H. Olivier, and K. Heufer, Transition to turbulence in hypersonic flow over a compression ramp due to intrinsic instability, J. Fluid Mech. **941**, A8 (2022).

[30] M. Lugrin, F. Nicolas, N. Severac, J. Tobeli, S. Beneddine, E. Garnier, S. Esquieu, and R. Bur, Transitional shockwave/boundary layer interaction experiments in the R2Ch blowdown wind tunnel, Exp. Fluids **63**, 46 (2022).

[31] P. Paredes, A. Scholten, M. Choudhari, F. Li, E. Benitez, and J. Jewell, Boundary-layer instabilities over a cone-cylinder-flare model at Mach 6, AIAA J. **60**, 5652 (2022).

[32] A. Dwivedi, G. Sidharth, and M. Jovanovic, Oblique transition in hypersonic double-wedge flow, J. Fluid Mech. **948**, A37 (2022).

[33] E. Benitez, J. Jewell, and S. Schneider, Separation bubble variation due to small angles of attack for an axisymmetric model at Mach 6, in *AIAA Scitech 2021 Forum, Virtual Event* (AIAA, 2021).

[34] E. Benitez, Instability measurements on two cone-cylinder-flares at Mach 6, Ph.D. thesis, Purdue University, West Lafayette, IN, 2021.

[35] T. Juliano, E. Swanson, and S. Schneider, Transition research and improved performance in the Boeing/AFOSR Mach-6 quiet tunnel, in *45th AIAA Aerospace Sciences Meeting and Exhibit, Reno, NV* (AIAA, 2007).

[36] S. Schneider, Development of hypersonic quiet tunnels, J. Spacecr. Rockets **45**, 641 (2008).

[37] S. Schneider, Developing mechanism-based methods for estimating hypersonic boundary-layer transition in flight: The role of quiet tunnels, J. Spacecr. Rockets **72**, 17 (2015).

[38] S. Esquieu, E. Benitez, S. Schneider, and J. Brazier, Flow and stability analysis of a hypersonic boundary-layer over an axisymmetric cone-cylinder-flare configuration, in *AIAA Scitech 2019 Forum, San Diego, CA* (AIAA, 2019).

[39] K. Casper, Pressure fluctuations beneath instability wave packets and turbulent spots in a hypersonic boundary layer, Ph.D. thesis, Purdue University, West Lafayette, IN, 2012.

[40] M. Wason, Calibration of high-frequency pressure sensors using low-pressure shock waves, Master's thesis, Purdue University, West Lafayette, IN, 2019.

[41] T. Juliano, L. Paquin, and M. Borg, HIFiRE-5 boundary-layer transition measured in a Mach-6 quiet tunnel with infrared thermography, AIAA J. **57**, 2001 (2019).

[42] J. Edelman, Nonlinear growth and breakdown of the hypersonic crossflow instability, Ph.D. thesis, Purdue University, West Lafayette, IN, 2019.

[43] G. Smeets and A. George, Gas-dynamic investigations in a shock tube using a highly sensitive interferometer, Tech. Rep. No. 14/71, translated by A. Goetz, Institut Saint-Louis, France, 1971.

[44] G. Smeets and A. George, Laser-interferometer with phase compensation, Tech. Rep. No. 28/73, translated by A. Goetz, Institut Saint-Louis, France, 1973.

[45] G. Smeets and A. George, Laser-differential interferometer applications in gas dynamics, Tech. Rep. No. R136/75, translated by A. Goetz, Institut Saint-Louis, France, 1975.

[46] G. Smeets, Laser interferometer for high sensitivity measurements on transient phase objects, IEEE Trans. Aerosp. Electron. Syst. **8**, 186 (1972).

[47] G. Smeets, Flow diagnostics by laser interferometry, IEEE Trans. Aerosp. Electron. Syst. **13**, 82 (1977).

[48] N. Parziale, J. Shepherd, and H. Hornung, Reflected shock tunnel noise measurement by focused differential interferometry, in *42nd AIAA Fluid Dynamics Conference and Exhibit, New Orleans, LA* (AIAA, 2012).

[49] N. Parziale, Slender-body hypervelocity boundary-layer instability, Ph.D. thesis, California Institute of Technology, Pasadena, CA, 2013.

[50] N. Parziale, J. Shepherd, and H. Hornung, Observations of hypervelocity boundary-layer instability, J. Fluid Mech. **781**, 87 (2015).

[51] J. Gladstone and T. Dale, Researches on the refraction, dispersion, and sensitiveness of liquids, Proc. R. Soc. London **12**, 317 (1863).

[52] A. Ceruzzi, C. Neisess, B. McManamen, and C. Cadou, Investigation of focused laser differential interferometry (FLDI) sensitivity function, in *AIAA Scitech 2021 Forum, Virtual Event* (AIAA, 2021).

[53] E. Benitez, M. Borg, J. Hill, M. Aultman, L. Duan, C. Running, and J. Jewell, Quantitative focused laser differential interferometry with hypersonic turbulent boundary layers, Appl. Opt. **61**, 9203 (2022).

[54] E. Benitez, J. Jewell, and S. Schneider, Focused laser differential interferometry for hypersonic flow instability measurements with contoured tunnel windows, in *AIAA Scitech 2020 Forum, Orlando, FL* (AIAA, 2020).

[55] E. Benitez, J. Jewell, and S. Schneider, Focused laser differential interferometry with contoured tunnel windows, AIAA J. **59**, 419 (2021).

[56] E. Benitez, M. Borg, C. Rhodes, and J. Jewell, Optical-axis spatial sensitivity of a simulated focused laser differential interferometer, AIAA J. **61**, 1925 (2023).

[57] K. Gray, Instability and transition on slender cones under fully quiet Mach-6 flow, Ph.D. thesis, Purdue University, West Lafayette, IN, 2022.

[58] A. Federov, Receptivity of a high-speed boundary layer, J. Fluid Mech. **491**, 101 (2003).

[59] J. Schaefer and H. Ferguson, Investigation of separation and associated heat transfer and pressure distribution on cone-cylinder-flare configurations at Mach five, ARS J. **32**, 762 (1962).

[60] D. Needham and J. Stollery, Boundary layer separation in hypersonic flow, in *3rd and 4th Aerospace Sciences Meeting, New York, NY* (AIAA, 1966).

[61] Y. Kim and E. Powers, Digital bispectral analysis and its applications to nonlinear wave interactions, IEEE Trans. Plasma Sci. **7**, 120 (1979).

[62] S. Elgar and G. R.T., Statistics of bicoherence, IEEE Trans. Acoustics Speech Signal Proc. **36**, 1667 (1988).

[63] E. Benitez, M. Borg, A. Scholten, P. Paredes, Z. McDaniel, and J. Jewell, Instability and transition onset downstream of a laminar separation bubble at Mach 6, J. Fluid Mech. **969**, A11 (2023).

[64] See Supplemental Material at http://link.aps.org/supplemental/10.1103/PhysRevFluids.8.083903 for videos of 0.05 seconds of flow at a variety of unit Reynolds numbers collected at 20 000 frames per second under both quiet and conventional-noise flow, highlighting the lack of large-scale spatial fluctuations in the shear layer under quiet flow.